

Millimetre-Wave and Near-Infrared Signposts of Massive Molecular Clump Evolution and Star Cluster Formation

Peter J. Barnes^{1*}, Stuart D. Ryder², Stefan N. O’Dougherty¹, Luis E. Alvarez¹,
Adriana S. Delgado-Navarro¹, Andrew M. Hopkins², and Jonathan C. Tan¹

¹*Astronomy Department, University of Florida, Gainesville, FL 32611, USA*

²*Australian Astronomical Observatory, PO Box 915, North Ryde, NSW 1670, Australia*

Accepted 2013 April 3. Received 2013 March 27; in original form 2012 February 22

ABSTRACT

We report new near-infrared and mm-wave observational data on a selection of massive Galactic molecular clumps (part of the CHaMP sample) and their associated young star clusters. The clumps show, for the first time in a “dense gas tracer”, a significant correlation between HCO⁺ line emission from cold molecular gas and Br γ line emission of associated nebulae. This correlation arises in the HCO⁺ line’s brightness, not its linewidth. In contrast, the correlation between the N₂H⁺ line emission and Br γ is weak or absent. The HCO⁺/N₂H⁺ line ratio also varies widely from clump to clump: bright HCO⁺ emission tends to be more closely associated with Br γ nebulosity, while bright N₂H⁺ emission tends to avoid areas that are bright in Br γ . Both molecular species show correlations of weak significance with infrared H₂ $v=1\rightarrow 0$ and $v=2\rightarrow 1$ line emission, in or near the clumps. The H₂ emission line ratio is consistent with fluorescent excitation in most of the clumps, although thermal excitation is seen in a few clumps. We interpret these trends as evidence for evolution in the gas conditions due to the effects of ongoing star formation in the clumps, in particular, the importance of UV radiation from massive YSOs as the driving agent that heats the molecular gas and alters its chemistry. This suggests that some traditional dense gas tracers of molecular clouds do not sample a homogeneous population of clumps, i.e., that the HCO⁺ brightness in particular is directly related to the heating and disruption of cold gas by massive young stars, whereas the N₂H⁺ better samples gas not yet affected by this process. We therefore suggest that the HCO⁺–N₂H⁺–Br γ relationship is a useful diagnostic of a molecular clump’s progress in forming massive stars.

Key words: astrochemistry — infrared lines: ISM — ISM: clouds — ISM: molecules — radio lines: ISM — stars: formation.

1 INTRODUCTION

Our understanding of the most important processes in massive star and cluster formation is still very inadequate, despite much effort in the past decade (Beuther et al. 2007). While a number of important surveys have been completed, detailed multi-wavelength studies often suffer from small sample size (e.g., Pirogov et al. 2007; Higuchi et al. 2009), while larger surveys often suffer from various selection effects and limited wavelength coverage (e.g., Longmore et al. 2007; Wu et al. 2010). Thus, there is little agreement on the essential physical, chemical, and dynamical features of massive molecular clumps as they give rise to star clusters, or likewise on the evolution of molecular cores that make

massive stars. There are also enduring mysteries, such as the source of turbulence in massive molecular clouds (Nakamura & Li 2005, 2011; Matzner 2007).

In large part, progress in our understanding of massive molecular clump evolution and cluster formation has been hindered by the triple obstacles of (i) large distances due to their relative rarity, (ii) their rapid evolution, and (iii) the rich variety of phenomena (masers, outflows, HII regions, a high density of objects) that luminous sources exhibit, and which a paradigm of massive star formation must account for. These obstacles make conducting large-scale, high-resolution and -sensitivity surveys difficult and time-consuming. Recently, however, a number of star formation surveys in the Milky Way have been undertaken, such as GLIMPSE (Benjamin et al. 2003), BGPS (Aguirre et al. 2011), Hi-GAL (Molinari et al. 2010), and several oth-

* E-mail: pjb@astro.ufl.edu

ers, that are at last providing the resolution, sensitivity, and statistical basis for a more thorough understanding of this problem. While these mainly broadband surveys are indeed transformative, rarer molecular-spectroscopic data from surveys such as CHaMP (described next) can provide even keener insights into massive molecular clump evolution.

2 OBSERVATIONS

2.1 The CHaMP Sample

The results reported here were obtained as part of the Galactic *Census of High- and Medium-mass Protostars* (CHaMP; Yonekura et al. 2005; Barnes et al. 2010, 2011). This is a complete, unbiased, multi-wavelength survey of massive, dense molecular clumps and associated young star clusters within a $20^\circ \times 6^\circ$ sector of the southern Milky Way. CHaMP’s main objectives are to systematically characterise the physical processes and timescales in massive star and cluster formation. The first complete catalogues and results of this project were presented by Barnes et al. (2011, hereafter Paper I). Here, 209 parsec-scale “Nanten clumps” were identified from 4’-resolution maps in the $J = 1 \rightarrow 0$ transitions of $C^{18}O$ and HCO^+ at $\lambda = 3$ mm wavelength: these comprise the Nanten Master Catalogue (hereafter NMC), denoted by their catalogue numbers (e.g., BYF 73). The brightest 121 of these were mapped at 40’’ resolution using the Mopra telescope (see §2.3 for more details) to resolve the molecular emission into sub-parsec-scale “Mopra clumps,” denoted by subcomponents of the NMC (e.g., BYF 77a). The powerful Mopra backend maps many molecular species simultaneously: over the initial observed range of 85–93 GHz, the brightest of these is the HCO^+ line, and analysis of the Mopra HCO^+ maps yielded the 303 entries in the catalogue of massive, dense clumps in Paper I (hereafter MHC, for Mopra HCO^+ Catalogue). Other species mapped are as listed in Table 3 of Paper I, and the analysis of these will appear in future papers. Among these, the species N_2H^+ and HCN are also fairly bright, but much less widespread than HCO^+ . Physically, N_2H^+ and HCN should trace similar conditions to HCO^+ , but their abundances are thought to depend on astrochemical factors (e.g., Caselli et al. 2002).

The main results of Paper I include: (i) the first recognition that the Milky Way’s dense molecular ISM is dominated by a vast, subthermally-excited population of massive clumps, which significantly outnumber the brighter and traditionally better-studied star forming regions; (ii) if the clumps evolve by slow contraction, up to 95% of this population may represent a long-lived stage of pressure-confined, gravitationally stable massive clump evolution, and the CHaMP clump population may not engage in vigorous massive star formation until the last 5% of their lifetimes; (iii) the brighter sources are denser, more massive, more highly pressurised, and closer to gravitational instability than the less bright sources. The MHC clumps’ properties are: integrated line intensity 1–30 K km s⁻¹, peak line brightness 1–7 K, linewidth 1–10 km s⁻¹, integrated line luminosity 0.5–200 K km s⁻¹ pc², size 0.2–2.5 pc, mean projected axial ratio 2, optical depth 0.08–2, surface density 30–3000 M_⊙ pc⁻², number density 0.2–30 × 10⁹ m⁻³, mass 15–8000 M_⊙, virial parameter 1–55, and gas pressure 0.3–700 pPa.

Paper I has therefore already provided a significant and

Table 1. AAT Observing Log.

UT Date	Field ^a	Filters
2006 May 13	BYF 40	all narrow
2006 May 13	BYF 54	all narrow
2006 May 13	BYF 73 ^b	all narrow
2006 May 13	BYF 77	all narrow
2006 May 13	BYF 128	all narrow
2007 May 26	BYF 66	all narrow
2011 Feb 18	BYF 5	Br γ , K -cont
2011 Feb 18	BYF 60	all narrow+broad
2011 Feb 18	BYF 61	all narrow+broad
2011 Feb 18	BYF 62	all narrow+broad
2011 Feb 18	BYF 63	all narrow+broad
2011 Feb 18	BYF 64	all narrow+broad
2011 Feb 18	BYF 83	all narrow+broad
2011 Feb 18	BYF 85	all narrow+broad
2011 Feb 18	BYF 118	all narrow+broad
2011 Feb 18	BYF 123	all narrow+broad
2011 Feb 18	BYF 208	all narrow+broad
2011 Mar 21	BYF 66	all narrow+broad
2011 Mar 23	BYF 67	all narrow+broad
2011 Mar 23	BYF 68	all narrow+broad
2011 Mar 23	BYF 69	all narrow+broad
2011 Mar 23	BYF 71	all narrow+broad
2011 Mar 24	BYF 72	all narrow+broad
2011 Mar 24	BYF 73	all narrow+broad
2011 Mar 24	BYF 76	all narrow+broad
2011 Mar 24	BYF 77	Br γ , H ₂ $v=1 \rightarrow 0$, K -cont

^a From the Nanten Master Catalogue in Paper I.

^b Analysed by Barnes et al. (2010).

well-advanced component of CHaMP, devoted to molecular spectroscopic mapping of these clumps at 3 mm wavelength, but the planned coverage of these clouds at other wavelengths is still in its early stages (e.g., Barnes et al. 2010). Nevertheless, from among this sample of star-forming clouds, we can already discern new insights from near-infrared (NIR) imaging of a subset of these clumps, and from a comparison of these images with selected mm-wave molecular maps. In order to statistically characterise the major stages of massive star and cluster formation, starting from the cold, prestellar gas stages and proceeding to the newly-emerged pre-MS stars, we need both a suitable sample of objects and a judicious choice of probes. Here we compare, for a subset of 60 members of the NMC, the HCO^+ maps from Paper I together with companion N_2H^+ maps presented here for the first time, plus new near-IR images which we describe next. As explained below, this subset of the CHaMP sample provides a good representation of the range of clump parameters contained in the MHC.

2.2 Near-IR Imaging

Being a hydrogen recombination line, Brackett γ naturally traces HII regions, i.e. ionised gas at temperatures ~ 7 –9,000 K. However, being in the NIR, Br γ is far less affected by dust extinction than the traditional optical tracer of ionised hydrogen, H α . Radio recombination lines (RRLs) are completely unaffected by dust extinction, however traditional surveys of cm-wave RRLs are still not sensitive to

the youngest Compact and Ultracompact HII regions, since the optical depth to free-free emission in such objects may be quite high. Thus, Br γ can conveniently probe the earliest stages of HII region formation around very young, deeply embedded massive stars that H α and cm-wave RRL surveys (for example) may simply be unable to see. Similarly, NIR H $_2$ lines sample regions where the molecular hydrogen has been heated (whether by shocks or fluorescence) to temperatures $\sim 1\text{--}4,000$ K. Thus, these lines can potentially probe gas which has been warmed, but not yet ionised, by the radiation from very young stars. Such line imaging has been used to study a number of Galactic star-forming regions (e.g., Caratti o Garatti et al. 2006), and recently a H $_2$ $v=1\rightarrow 0$ survey of more than half of the Milky Way’s first quadrant has been completed (Fröbrich et al. 2011). But apart from a few such studies, remarkably little systematic, large-scale, near-IR survey work of the kind described in this paper has been performed.

We obtained near-IR images of 26 fields, of which 22 are non-redundant, covering 60 CHaMP clumps (about 20% of the MHC) using the IRIS2 camera (Tinney et al. 2004) on the Anglo-Australian Telescope (Table 1). We began with a pilot study using AAT service time in 2006 and 2007, obtaining images of 6 clumps using only the narrowband filters (fractional bandwidths $\sim 1.4\%$) for the emission lines Br γ ($\lambda = 2.17\mu\text{m}$), H $_2$ $v=1\rightarrow 0$ $S(1)$ ($2.12\mu\text{m}$) and $v=2\rightarrow 1$ $S(1)$ ($2.25\mu\text{m}$), plus a fourth “ K -continuum” narrowband filter in a line-free part of the band ($2.25\text{--}2.28\mu\text{m}$, although this filter may still contain some residual emission from the $v=2\rightarrow 1$ line). As these filters all lie in the K -band, the differential reddening between them should be minimal.¹ The observation and data reduction procedures were as described by Barnes et al. (2010). Briefly, for each filter $9 \times 60\text{s}$ images (dithered by $1'$) were obtained of the instrument’s 7.7×7.7 field under $0''.9$ seeing, and reduced using the ORAC-DR pipeline (Cavanagh et al. 2003). Subsequent image processing was performed with the IRAF² and MIRIAD (Sault et al. 1995) packages. After astrometric registration using SuperCOSMOS³ I -band images, we linearly scaled the spectral-line images to the same relative brightness scale as the K -band continuum by matching the integrated fluxes of several stars in each filter, assuming they were of similar colour. We then subtracted the continuum from the spectral-line images before transforming each image to Galactic coordinates. Finally, pseudo-colour images (described in §3.1) were formed from these line images.

In 2011 over 8 nights with variable conditions, we obtained (in the periods when the sky was clear) similar nar-

rowband images of the other fields in Table 1, plus JHK broadband images. In this season, however, 3 of the narrowband images were made with $5 \times 60\text{s}$ dithers each, while the $v=2\rightarrow 1$ imaging used $5 \times 120\text{s}$ dithers to compensate for the generally fainter emission seen previously in this line; the broadband images were each constructed from $5 \times 10\text{s}$ dithers. Thus, the pilot K -cont, Br γ , and $v=1\rightarrow 0$ images from 2006–07 are more sensitive than the equivalent 2011 data. The ORAC-DR pipeline for the 2011 observations included astrometric registration using 2MASS⁴ JHK catalogue data, resulting in alignments good to $\sim 1''$ (no further astrometry with SuperCOSMOS was performed here). Otherwise the reduction procedures used were as above. In what follows we discuss only the narrowband images, and leave the analysis of the broadband emission for a later study.

From the above, while it is clear that the fields covered by this IR imaging were not systematically optimised for (e.g.) uniformity, brightness, or other property (due primarily to the vagaries of observing conditions), the resulting dataset nevertheless yields a useful microcosm of the MHC: for example, the 2006–07 data cover many of the brighter clumps, while the 2011 data cover most of “Region 9” from Paper I. We can therefore reliably examine here a range of clumps from the brightest and most massive to the relatively large fraction of fainter and more moderate-mass clouds.

2.3 Mopra Mapping

At lower temperatures, H $_2$ is spectroscopically inert: to probe this cold gas, we must turn to trace species. The CO molecule and its isotopologues are bright and widely-used, yet they typically represent the lower-density envelopes of molecular clouds (number densities $\sim 10^{8\text{--}9}\text{ m}^{-3}$ or less, corresponding to mass densities $\sim 60\text{ M}_\odot\text{ pc}^{-3}$). In contrast, most star formation is known to occur in only the denser cores and clumps of these clouds, with densities at least 10 times higher (Lada & Lada 2003). Instead, HCO $^+$ and N $_2$ H $^+$ are useful higher-density cold gas probes expected to trace similar physical conditions in the molecular gas: both are ions with large dipole moments and similar excitation requirements, sensitive to densities $\sim 10^{10}\text{ m}^{-3}$ or more.

We obtained maps of the HCO $^+$ and N $_2$ H $^+$ $J = 1 \rightarrow 0$ emission at 89.188526 and 93.173777 GHz (resp.) using the 22 m diameter Mopra antenna, part of the Australia Telescope National Facility⁵. Mopra’s MOPS spectrometer collects data on multiple molecular species simultaneously, therefore the relative registration of features in maps of the two molecular species is perfect. The absolute pointing accuracy was set by \sim hourly checks on the SiO maser source R

¹ The labels for the two H $_2$ filters were inadvertently switched in Figure 7a of Barnes et al. (2010), but the error does not affect the conclusions of that work. This labelling error has been corrected here.

² IRAF is distributed by the National Optical Astronomy Observatories, which are operated by the Association of Universities for Research in Astronomy, Inc., under cooperative agreement with the U.S. National Science Foundation.

³ This research has made use of data obtained from the SuperCOSMOS Science Archive, prepared and hosted by the Wide Field Astronomy Unit, Institute for Astronomy, University of Edinburgh, which is funded by the UK Science and Technology Facilities Council.

⁴ This publication makes use of data products from the Two Micron All Sky Survey, which is a joint project of the University of Massachusetts and the Infrared Processing and Analysis Center/California Institute of Technology, funded by the National Aeronautics and Space Administration and the National Science Foundation.

⁵ The Mopra telescope is part of the Australia Telescope which is funded by the Commonwealth of Australia for operation as a National Facility managed by CSIRO. The University of New South Wales Digital Filter Bank used for the observations with the Mopra telescope was provided with support from the Australian Research Council.

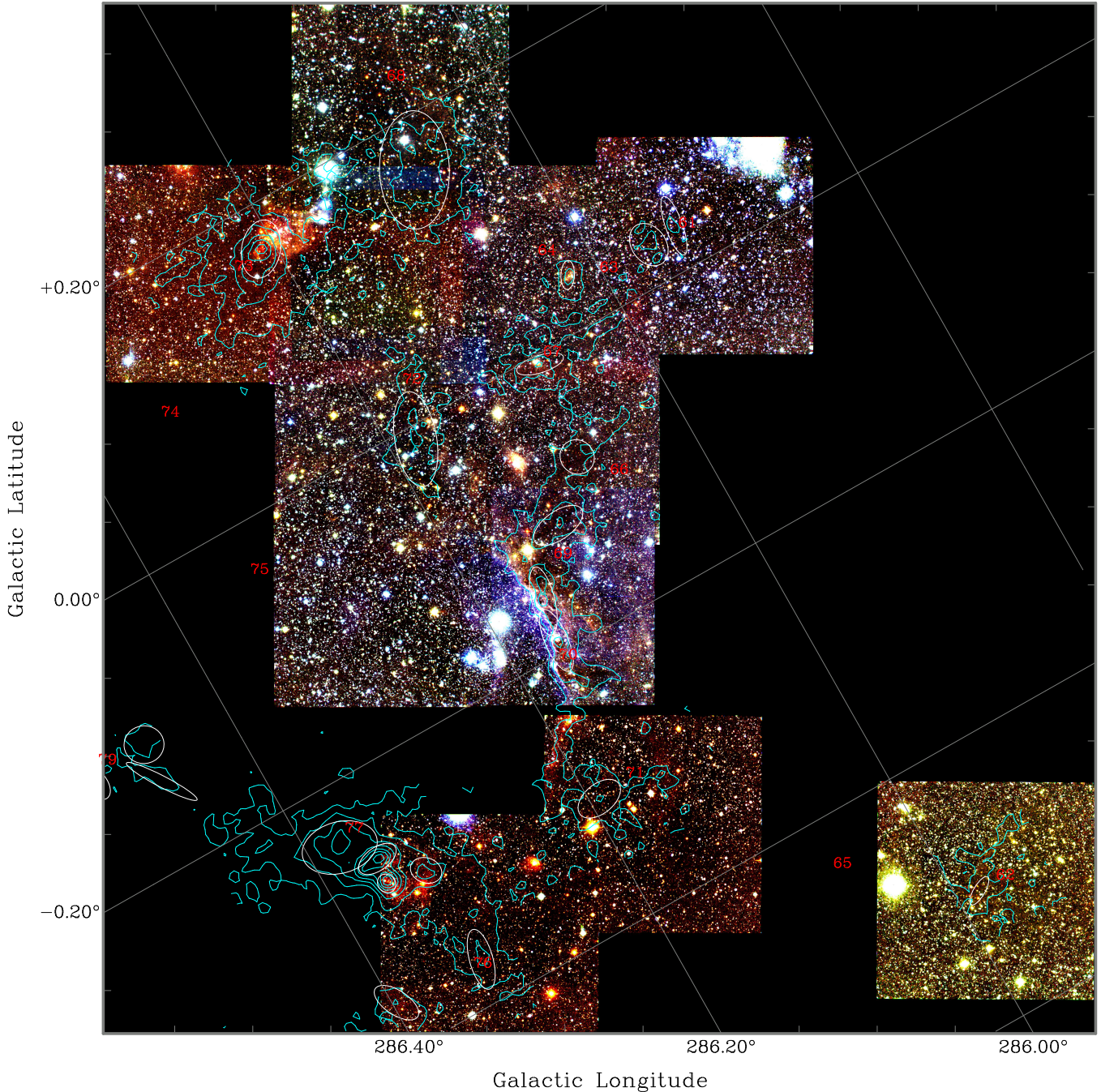


Figure 1. Wide-field RGB-pseudo-colour image of broad-band *JHK* for BYF 61–78 (most of Region 9 from Paper I) using mosaicked 2011 data, overlaid by Mopra HCO^+ contours (cyan levels at 5, 10, 15, 20, 25, 30, and 35 times the rms level of $0.404 \text{ K km s}^{-1}$). The white ellipses show gaussian fits to the HCO^+ emission, while the red numbers indicate nominal positions of NMC clumps. This figure is provided for the convenience of locating the fields of Figs. A5–A16 in their wider context — compare this image with Fig. 34 in Paper I. At a distance of 2.5 kpc, the scale is $40'' = 0.485 \text{ pc}$ or $1 \text{ pc} = 0^{\circ}0229 = 82''5$.

Carinae, and was generally found to be better than $10''$. Full details of the hardware, mapping, and data reduction procedures are given in Paper I, and the HCO^+ maps are drawn from that catalogue. The N_2H^+ maps presented here are new, but have been produced in the same way as the HCO^+ maps of Paper I. Therefore, details of the N_2H^+ data such as beam size (HPBW $\sim 40''$), noise characteristics (global average $T_{\text{rms}} \sim 0.31 \text{ K}$ per 0.11 km s^{-1} channel), and the like, are virtually identical to those for HCO^+ in Paper I.

3 IMAGES AND ANALYSIS

3.1 General Features

Of the 22 fields imaged and reported here, 12 comprise a large part of Region 9 from Paper I, while the other 10 fields variously cover some of the brighter and fainter clumps from the MHC. We first present in Figure 1 a wide-field, *JHK* broadband mosaic of the twelve Region 9 fields, to provide

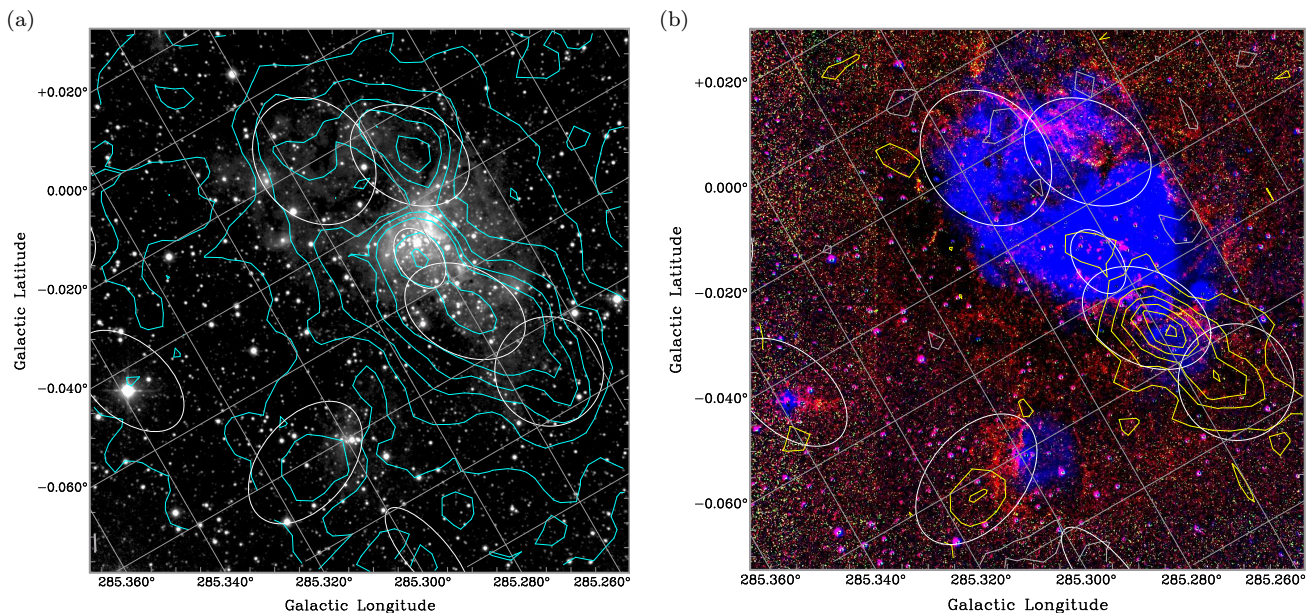


Figure 2. Example of the survey fields presented in the Appendix (available online only). These images of BYF 54 (part of Region 8 from Paper I) are from the more sensitive 2006 data. (a) K -band line-free continuum image on a linear brightness scale. Contours are overlaid from Mopra HCO^+ integrated intensity: cyan levels at 4, 8, 12, 16, 20, 24, 40, and 56 times the rms at $0.401 \text{ K km s}^{-1}$. (b) RGB-pseudo-colour image of the continuum-subtracted K -band spectral lines on a linear brightness scale. Here, $\text{H}_2 S(1)$ is shown as red ($v=1 \rightarrow 0$) & green ($v=2 \rightarrow 1$), while $\text{Br}\gamma$ is shown as blue. Overlaid here are contours of Mopra N_2H^+ integrated intensity (grey levels at ~ 2 , and yellow levels at 2, 4, 6, 8, 10, and 12 times the rms of $0.603 \text{ K km s}^{-1}$). The white ellipses represent gaussian fits to the HCO^+ emission in both panels. At a distance of 2.5 kpc, the scale is $40'' = 0.485 \text{ pc}$ or $1 \text{ pc} = 0^\circ 0229 = 82''.5$. This field shows perhaps the most obvious example of the $\text{HCO}^+/\text{N}_2\text{H}^+$ intensity variations with position, as described in §3.2ff.

a wider context for the individual fields described next. In Figure 2 we give a sample narrowband field showing the salient features of our presentation, while all the available narrowband IR images are presented in the Appendix (Figures A1–A22).

In each individual field (see Fig. 2), we show the line-free K -continuum in the left panel, and a pseudo-colour composite image of the continuum-subtracted line emission in the right panel, where (except in Fig. A1) the $\text{H}_2 v=1 \rightarrow 0$ and $v=2 \rightarrow 1$ are shown as red and green, respectively, while $\text{Br}\gamma$ is shown as blue. These colours therefore represent the excitation level in the gas: where only $\text{H}_2 v=1 \rightarrow 0$ exists at gas temperatures $\sim 1,000\text{--}2,000 \text{ K}$, we see red nebulosity, through yellow or green areas where the $v=2 \rightarrow 1$ emission picks up or dominates at $\sim 2,000\text{--}4,000 \text{ K}$, to cyan or blue areas where the $\text{Br}\gamma$ shows ionised gas at $\sim 7,000\text{--}9,000 \text{ K}$. (The colour stretches in each Figure, however, are not the same, and are chosen to display the most information in each panel.) In addition, the panels are overlaid by contours of the integrated intensity of the two molecular species HCO^+ (cyan contours, usually in the K -cont panel) and N_2H^+ (yellow contours, usually in the line emission panel where available). In some figures, both sets of contours are overlaid on each panel. We also show in both panels (as white ellipses) gaussian fits to the components of the HCO^+ emission only, which help to register features between the panels.

While these figures show a wide variety of stellar groupings and emission-line morphologies, there are a few trends in common, which we now explore. First, we note a somewhat subtle point: IR emission tends to be absent or very weak in the clumps with relatively weaker mm-line emis-

sion. In other words, stronger IR emission tends to occur with stronger mm-line emission, and there may be a distinct threshold of mm emission needed before IR line emission becomes apparent at these levels. A second trend is more prominent: the IR emission lines tend to be spatially quite distinct, i.e. the HII regions (as traced by the $\text{Br}\gamma$) rarely overlap with the H_2 emission, although they are frequently adjacent. Also, the HII emission is always relatively diffuse, although sometimes a sharp ionisation front is visible (e.g., BYF 70). In contrast, the H_2 emission is usually (but not always) quite filamentary, with widths often as small as a few arcseconds but lengths up to an arcminute or more (e.g., in or near clumps BYF 54d, 73, 77a,c; the clump designations are given in Table 4 and Appendix A of Paper I). Where diffuse (i.e., non-filamentary) H_2 emission is occasionally seen, it is almost always centred on one of the stars embedded in the cold gas clump (e.g., BYF 40a, 77a). In general, then, there is a high coincidence of $\text{Br}\gamma$ and H_2 emission from within and around the brighter examples of these cold, massive, dense clumps.

As for the clumps themselves, the HCO^+ and N_2H^+ also show interesting relationships. Overall, the N_2H^+ follows the HCO^+ distribution reasonably well, although typically it is $\sim 2\text{--}5$ times fainter. In detail, however, the two species differ. Often the $\text{HCO}^+/\text{N}_2\text{H}^+$ brightness ratio (hereafter η) varies markedly across adjacent clumps. A very clear example of this is in BYF 54 (Fig. 2), where the ratio drops from ~ 14 to 2.1 to 1.7 going from clumps 54a to 54b to 54c, but the trend is evident in many other locations as well.

When we now intercompare the trends seen in the IR and mm line ratios, we obtain a remarkable result: the

Table 2. Mopra N₂H⁺ $J = 1 \rightarrow 0$ Observed Parameters.

BYF no.	l deg	b deg	$\int T_R^* dV$ K km s ⁻¹	V range km s ⁻¹	T_p K	V_{LSR} km s ⁻¹	σ_V km s ⁻¹	$\sigma_{V,dec}$ km s ⁻¹	θ_{maj} arcsec	θ_{min} arcsec	PA deg
5a	280.988	-1.537	1.56(22)	-12.0,-2.0	0.62(21)	-7.6 (11)	1.39 (9)	1.26 (9)	143(12)	46(16)	104(3)
5b	N	N	- (38)	-12.0,-2.0	- (37)	-	-	-	-	-	-
5c	281.034	-1.505	0.85(21)	-12.0,-2.0	0.64(20)	-7.25(11)	1.54 (3)	1.42 (3)	116(13)	<46	11(5)
5d	281.048	-1.540	0.80(21)	-12.0,-2.0	0.66(20)	S	S	S	45(16)	<46	143(5)
7a	281.074	-1.570	0.84(23)	-12.0,-2.0	0.66(22)	-6.4 (10)	0.80(25)	0.55(25)	64(14)	<47	108(5)
40a	284.017	-0.871	4.20(24)	+6.0,+12.0	1.53(30)	+8.58(12)	1.39(11)	1.26(11)	95(13)	36(18)	144(3)
40b	284.036	-0.893	3.20(23)	+6.0,+12.0	1.36(28)	+8.88(15)	1.19 (8)	1.04 (8)	74(14)	45(16)	90(3)
40c	284.019	-0.899	1.41(24)	+6.0,+12.0	1.06(29)	+8.5 (6)	1.0 (6)	0.8 (6)	<52	<40	-
40d	283.989	-0.836	0.94(23)	+6.0,+12.0	0.93(28)	+9.2 (5)	2.06 (9)	1.98 (9)	<38	<30	124(5)
40e	N	N	- (20)	+6.0,+12.0	- (24)	-	-	-	-	-	-
40f	284.052	-0.836	0.73(22)	+6.0,+12.0	0.77(27)	+8.2 (10)	1.3 (5)	1.2 (5)	<38	<30	56(5)
40g	N	N	- (24)	+6.0,+12.0	- (30)	-	-	-	-	-	-
54a	285.266	-0.047	0.95(27)	-1.0,+6.0	0.89(31)	+3.25(23)	2.06(10)	1.98(10)	<30	<30	72(5)
54b	285.257	-0.073	4.87(30)	-1.0,+6.0	1.93(35)	+2.75(15)	1.30(18)	1.16(18)	57(15)	<30	31(3)
54c	285.251	-0.090	3.25(30)	-1.0,+6.0	1.40(34)	+4.04(31)	0.63(31)	0.39(31)	51(15)	51(15)	0(5)
54d	285.261	-0.037	0.94(27)	-1.0,+6.0	0.81(31)	+3.6 (5)	1.7 (5)	1.6 (5)	57(15)	<30	121(5)
54e	285.261	-0.007	1.25(29)	-1.0,+6.0	1.03(34)	+4.10(25)	0.41(34)	0.39(34)	<45	<30	0(5)
54f	285.307	-0.077	1.08(29)	-1.0,+6.0	0.93(33)	+2.1 (5)	2.51 (5)	2.44 (5)	36(18)	31(20)	117(5)
54g	N	N	- (46)	-1.0,+6.0	- (53)	-	-	-	-	-	-
54h	N	N	- (26)	-1.0,+6.0	- (30)	-	-	-	-	-	-
61a	N	N	- (20)	-25.0,-19.0	- (25)	-	-	-	-	-	-
61b	N	N	- (21)	-25.0,-19.0	- (26)	-	-	-	-	-	-
62	N	N	- (36)	-25.0,-19.0	- (45)	-	-	-	-	-	-
63	286.020	+0.040	0.92(23)	-25.0,-19.0	0.80(28)	-22.48(25)	1.1 (5)	0.9 (5)	34(19)	<30	126(5)
64	N	N	- (24)	-25.0,-19.0	- (29)	-	-	-	-	-	-
66	286.090	-0.084	0.95(21)	-25.0,-19.0	0.56(26)	-21.4 (6)	1.73(15)	1.63(15)	64(14)	46(16)	108(5)
67	286.077	-0.020	0.74(24)	-25.0,-19.0	0.83(29)	S	S	S	51(15)	<30	68(5)
68	N	N	- (22)	-25.0,-19.0	- (27)	-	-	-	-	-	-
69	286.120	-0.120	1.16(24)	-25.0,-19.0	0.80(29)	-22.45(36)	0.96(25)	0.76(25)	95(13)	46(16)	126(3)
70a	286.147	-0.144	0.96(23)	-25.0,-19.0	0.88(29)	-22.76(39)	0.87(24)	0.64(24)	139(12)	<30	138(3)
70b	286.163	-0.190	1.31(19)	-25.0,-19.0	0.76(24)	-21.53(22)	1.44(34)	1.32(34)	46(16)	<47	101(5)
71	N	N	- (28)	-25.0,-19.0	- (34)	-	-	-	-	-	-
72	286.173	-0.007	0.91(22)	-25.0,-19.0	0.87(27)	-21.83(28)	1.20(22)	1.05(22)	112(13)	45(16)	135(5)
73	286.213	+0.166	4.87(20)	-25.0,-19.0	1.79(24)	-20.69(17)	0.93(14)	0.72(14)	61(14)	45(16)	99(3)
76	286.327	-0.360	0.83(24)	-25.0,-19.0	0.90(29)	-21.6 (9)	2.1 (9)	2.0 (9)	36(18)	<38	27(5)
77a	286.360	-0.280	4.54(20)	-25.0,-19.0	2.18(25)	-22.18(18)	1.07(10)	0.90(10)	45(16)	<38	37(3)
77b	286.353	-0.267	3.10(20)	-25.0,-19.0	1.63(25)	-22.18(15)	0.98(15)	0.79(15)	101(13)	<45	96(3)
77c	286.380	-0.237	1.53(20)	-25.0,-19.0	0.88(24)	-22.80(32)	1.85 (7)	1.76 (7)	101(13)	<45	84(3)
77d	286.330	-0.292	0.97(23)	-25.0,-19.0	0.90(28)	-21.30(31)	1.98(39)	1.89(39)	<47	<30	166(5)
78a	286.400	-0.357	0.82(24)	-25.0,-19.0	0.88(29)	-20.8 (9)	1.0 (5)	0.8 (5)	<30	<30	0(5)
78b	286.433	-0.390	0.81(25)	-25.0,-19.0	0.76(30)	-21.5 (9)	1.6 (5)	1.5 (5)	<49	<30	135(5)
78c	286.437	-0.437	0.98(24)	-25.0,-19.0	0.94(29)	-22.03(26)	1.80(11)	1.70(11)	<39	<30	198(5)
79a	N	N	- (24)	-25.0,-19.0	- (29)	-	-	-	-	-	-
79b	N	N	- (15)	-25.0,-19.0	- (19)	-	-	-	-	-	-
79c	286.513	-0.090	0.86(24)	-25.0,-19.0	0.85(29)	-22.11(33)	1.82(23)	1.72(23)	75(14)	<30	98(5)
83	286.959	-0.710	1.64(38)	-23.5,-12.9	0.99(33)	-17.6 (9)	1.17(22)	1.01(22)	<30	<30	0(5)
85a	N	N	- (28)	-23.5,-12.9	- (26)	-	-	-	-	-	-
85b	286.995	-0.083	1.46(35)	-23.5,-12.9	1.11(32)	-18.7(17)	1.3 (5)	1.1 (5)	75(14)	<30	172(3)
85c	N	N	- (32)	-12.9,-3.3	- (31)	-	-	-	-	-	-
117d	N	N	- (22)	-19.5,-15.5	- (33)	-	-	-	-	-	-
117e	288.190	-1.117	0.83(22)	-19.5,-15.5	0.79(33)	-17.90(20)	1.17 (8)	1.01 (8)	100(13)	<30	0(5)
118a	288.253	-1.140	2.72(22)	-19.5,-15.5	1.60(33)	-17.46(13)	0.83(10)	0.59(10)	55(15)	<49	45(3)
118b	N	N	- (19)	-19.5,-15.5	- (29)	-	-	-	-	-	-
118c	N	N	- (22)	-19.5,-15.5	- (33)	-	-	-	-	-	-

Table 2 – continued

BYF no.	l deg	b deg	$\int T_R^* dV$ K km s $^{-1}$	V range km s $^{-1}$	T_p K	V_{LSR} km s $^{-1}$	σ_V km s $^{-1}$	$\sigma_{V,dec}$ km s $^{-1}$	θ_{maj} arcsec	θ_{min} arcsec	PA deg
126a	291.267	-0.723	7.04(26)	-27.5,-21.0	2.99(30)	-23.72 (9)	1.19(14)	1.04(14)	>55	44(16)	45(5)
126b	N	N	– (37)	-27.5,-21.0	– (44)	–	–	–	–	–	–
126c	291.257	-0.767	6.40(28)	-27.5,-21.0	2.58(32)	-23.82(22)	1.19 (9)	1.04 (9)	>86	>64	120(5)
126d	N	N	– (47)	-27.5,-21.0	– (55)	–	–	–	–	–	–
126e	N	N	– (43)	-27.5,-21.0	– (50)	–	–	–	–	–	–
128a	291.313	-0.678	8.37(45)	-27.5,-21.0	2.77(53)	-24.61(19)	1.54(15)	1.43(15)	45(16)	<45	0(3)
128b	291.303	-0.702	2.61(48)	-27.5,-21.0	1.72(57)	-24.2 (6)	1.6 (4)	1.5 (4)	>107	36(18)	18(5)
208a	299.543	-0.341	0.94(20)	-41.5,-37.5	0.79(30)	-38.46(31)	0.74(31)	0.45(31)	153(12)	<30	81(3)
208b	299.536	-0.315	0.65(20)	-41.5,-37.5	1.03(30)	-38.2 (5)	S	S	>45	<30	143(5)

NOTES. An “N” in columns 2 & 3 and dashes in the other columns indicate clumps for which no N_2H^+ emission could be detected, with the rms sensitivity given in column 4. An “S” in columns 7–9 indicates clumps which were detected in N_2H^+ , but for which the S/N was too low to give reliable higher moment measurements. The values in column 9 are deconvolved from those in column 8, as described in the text. Uncertainties in parentheses are in the last digit of the corresponding value. Because they were mapped at Mopra in 2005 before the powerful MOPS spectrometer became available, clumps BYF 60a–b and 123a–d were not mapped in N_2H^+ , and so do not appear in this Table. They do appear below in Table 3 and in Paper I.

HCO^+ emission seems to be more strongly correlated with bright $Br\gamma$ emission, while bright N_2H^+ seems to avoid such areas of high ionisation. We further note that the $Br\gamma$ or H_2 emission is often (but not always) only associated with a single clump, or single interclump location. In some cases, a single gas clump is associated with both $Br\gamma$ and H_2 emission (e.g., BYF 54f), but then the IR lines are adjacent to each other, either on different sides of the clump, or separated by an apparent ionisation front. We examine these trends in more detail next.

3.2 Millimetre Data

The data analysis procedure for the mm lines has been described in Paper I. Briefly, each emission clump is characterised by its brightness, angular size, and velocity dispersion or linewidth. Then, whether one assumes an excitation temperature (T_{ex}) for the molecular emission (as was done in Paper I) or derives the T_{ex} from other mm-wave data, one can calculate (if the cloud’s distance and molecular abundance are known or assumed) a host of physical parameters, such as the radius, mass, density, etc., for the cold gas so traced. The HCO^+ data for these clouds were given in Paper I, and the observed data are given for the N_2H^+ maps in Table 2 in the same format as in Paper I, since we found that almost all of the N_2H^+ emission *structures* correlated very closely to the location of the HCO^+ clumps.

Because the $N_2H^+ J = 1 \rightarrow 0$ transition is split into 7 hyperfine components separated by a few km s $^{-1}$, measuring simple moments of the emission profiles in cold, dense clumps will not give the true V_{LSR} and σ_V values of the clumps. Approximately, when integrating over the central 3 hyperfine components ($F_1 = 2 \rightarrow 1$) as was done here, the V_{LSR} will be measured to be 0.20 km s $^{-1}$ too positive. Likewise for σ_V , the 3 hyperfine components can be treated as adding a dispersion of 0.58 km s $^{-1}$ in quadrature to the intrinsic value of the emission; the measured σ_V can then be corrected by inverting this effect. The reader should therefore note these approximate corrections to the *unmodified* moments compiled in Table 2 (columns 7, 8). While a full hyperfine treatment of *all* N_2H^+ maps is deferred to a later paper, the *corrected* N_2H^+ values (as described here) are

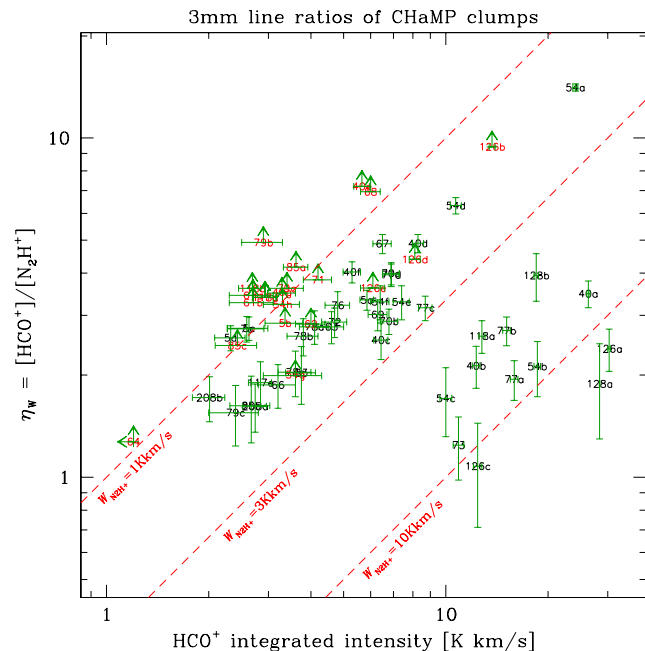


Figure 3. HCO^+ – N_2H^+ line intensity ratio η_W as a function of $W(HCO^+)$, labelled by clump number and overlaid by lines of constant $W(N_2H^+)$. Where shown, lower limits on η_W (shown with red labels) derive from upper limits on $W(N_2H^+)$ at 3 times the rms noise level.

given in Table 2, column 9 and analysed below (Figs. 10, 11, 13; §§3.4–4.1). These should be sufficiently close to the true values for the purposes of this comparative analysis.

Likewise, we also defer the calculation of physical parameters from the N_2H^+ maps, since these also need a full hyperfine analysis, and moreover, will depend strongly on the assumed molecular abundance $X(N_2H^+)$ of N_2H^+ relative to H_2 . It has already been shown in low-mass cores that $X(N_2H^+)$ is a strong function of CO-depletion processes in the cold gas (e.g., Caselli et al. 2002), and recent work suggests that a similar condition holds in higher-mass clumps

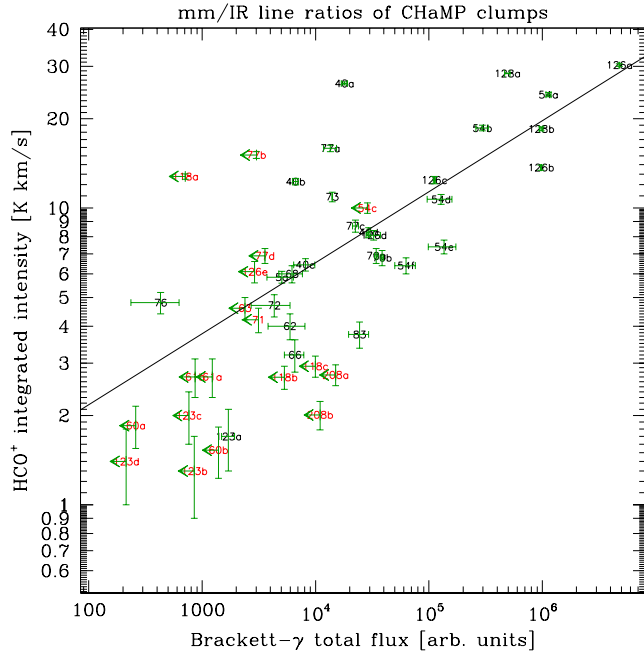


Figure 4. HCO^+ line intensity vs. $\text{Br}\gamma$ integrated flux, labelled by clump number. Black labels with green error bars denote clumps with reliable measurements in both lines, while red labels with green 3σ upper limits show clumps near which no $\text{Br}\gamma$ was detectable. Also shown is an unweighted least-squares fit to the well-measured points (black labels), with slope $m = 0.24 \pm 0.04$ and Pearson’s correlation coefficient $r^2 = 0.54$. The rms scatter about this trend is a factor of 1.6 in the ordinate (0.20 in $\log y$).

(e.g., Zinchenko et al. 2009). Therefore we cannot yet meaningfully discuss the physical conditions in the N_2H^+ emitting gas. Instead, we discuss below the relationship of N_2H^+ to the other tracers in the context of this understanding of the chemical origin and evolution of N_2H^+ .

3.3 IR Image Analysis

We measured the continuum-subtracted IR line emission as follows. For each field and filter, any IR line emission was first “assigned” to a particular clump. In most cases, clumps are sufficiently separated that this assignment was obvious, but in some areas (e.g., BYF 54 in Fig. 2) the IR emission extends broadly across multiple clumps. In these cases we used the gaussian ellipses fitted to the HCO^+ emission to divide the IR emission into non-overlapping areas associated with each clump. The basic idea is one of proximity: to which mm clump is the IR emission closest on the sky?

Once these assignments were made, we used the task CGCURS in MIRIAD to measure the IR lines’ mean brightness over the area assigned to each clump, and to record the area of integration. Then, one or two neighbouring emission-free areas in the image were also measured to find a suitable mean background brightness level. This background value was subtracted from the mean emission value, and the result multiplied by the size (in pixels) of the area integrated, to obtain a net line flux for each molecular clump. The results of these measurements are shown in Table 3.

Here we quote the IR line brightnesses on a relative scale. This scale was set by the analogue-to-digital

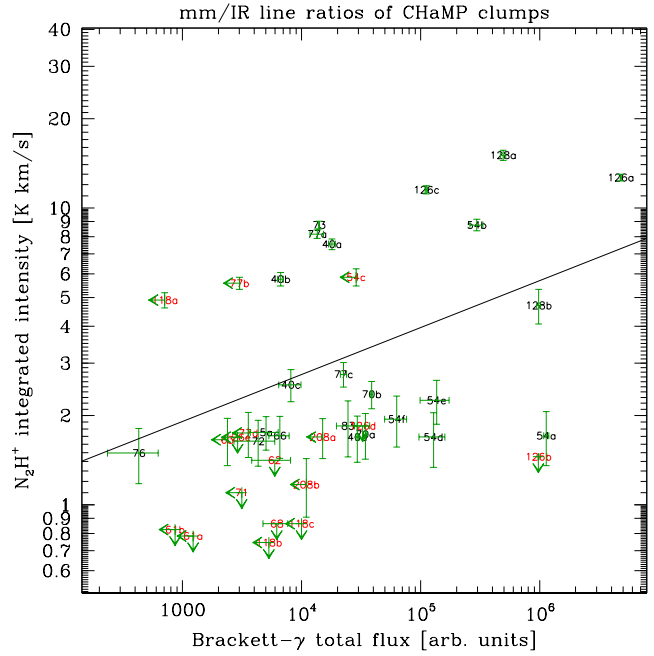


Figure 5. N_2H^+ line intensity (on the same ordinate scale as Fig. 4) vs. $\text{Br}\gamma$ integrated flux, labelled by clump number. Other details are as in Fig. 4. Here the unweighted least-squares fit to the well-measured points (black labels) has $m = 0.16 \pm 0.07$, $r^2 = 0.18$, and an rms scatter of 2.2 in the ordinate (0.35 in $\log y$).

units (ADU) conversion in the IRIS2 camera and ORAC-DR pipeline (see §2.2). In good conditions, this scale would normally be stable over the long- and short-term, resulting in well-calibrated images that could easily be converted to an absolute scale by a single numerical factor. Because of the rather variable sky conditions in the 2011 season, however, our calibration stability was less certain. To measure this, we examined our NIR data in two ways.

First, we compared the factors we derived for scaling the various narrowband filters to the K -cont filter in each observed field (i.e., prior to subtracting them from the continuum image). The mean \pm standard deviation scaling factors for the $\text{Br}\gamma$ and $\text{H}_2 v=1\rightarrow 0$ filters were 0.96 ± 0.06 and 0.96 ± 0.11 (resp.), while it was 0.54 ± 0.08 for $v=2\rightarrow 1$ (as expected for the doubled integration time in this filter). These factors represent good short-term stability in the calibration, considering the $\sim 40^m$ timescale for cycling through all filters in a given field.

Second, we compared the unscaled K -cont fluxes of several stars in each field to the K_s values from the 2MASS catalogue, in order to measure the longer-term calibration stability over the nights of observation. Averaged over all fields, we found a mean \pm standard deviation conversion of $(3.37 \pm 1.20) \times 10^5$ ADUs/Jy. Perhaps not surprisingly, this dispersion is larger than for the short-term, and means that the calibration between fields is less certain.

Nevertheless, we show below that this calibration uncertainty is well within the scatter of the results presented here. For example, the scatter in the IR line parameters is typically a factor of 4 or more; thus a calibration dispersion of 35%, while larger than desirable, cannot affect our results by a meaningful amount.

Table 3. AAT $2\mu\text{m}$ Narrowband Filters Observed Parameters.

BYF no.	Brackett- γ			H ₂ $v=1\rightarrow 0$			H ₂ $v=2\rightarrow 1$		
	Area	Net Mean	Net Flux	Area	Net Mean	Net Flux	Area	Net Mean	Net Flux
5a	8701	0.58(15)	5.0(13)	–	–	–	–	–	–
5b	–	–	–	–	–	–	–	–	–
5c	–	–	–	–	–	–	–	–	–
5d	–	–	–	–	–	–	–	–	–
7a	–	–	–	–	–	–	–	–	–
40a	8565	2.10(13)	18.0(11)	3196	1.066(37)	3.41(12)	9925	–0.112(71)	–
40b	2819	2.36(13)	6.66(37)	7427	4.222(37)	31.36(27)	2486	0.656(41)	1.63(10)
40c	12987	0.63(13)	8.1(17)	7017	1.691(37)	11.87(26)	1339	1.740(41)	2.330(55)
40d	6093	4.82(13)	29.38(81)	1183	0.881(37)	1.043(44)	1084	0.764(41)	0.828(45)
40e	–	–	–	–	–	–	–	–	–
40f	–	–	–	–	–	–	–	–	–
40g	–	–	–	–	–	–	–	–	–
54a	39131	29.0(15)	1134(57)	16593	2.269(7)	37.64(11)	24695	–1.941(8)	–
54b	25349	11.7(15)	296(37)	19841	0.722(7)	14.32(14)	15959	–0.735(8)	–
54c	8017	0.7(15)	5(12)	9973	0.368(7)	3.666(69)	14945	0.185(8)	2.77(12)
54d	21620	5.9(15)	128(32)	14170	0.651(7)	9.220(98)	17297	–0.498(8)	–
54e	25635	5.3(15)	136(37)	16856	0.471(7)	7.93(12)	20857	–0.802(8)	–
54f	8933	7.0(15)	63(13)	7778	1.162(7)	9.035(54)	9523	–0.195(8)	–
54g	–	–	–	–	–	–	–	–	–
54h	–	–	–	–	–	–	–	–	–
60a	1363	–0.153(64)	–	4144	22.31(14)	92.46(57)	6670	–0.15(98)	–
60b	7302	–0.087(64)	–	3660	23.31(14)	85.32(51)	5530	–0.06(98)	–
61a	13249	–0.058(31)	–	15264	0.0249(29)	0.381(45)	11150	0.016(13)	1.8(15)
61b	9337	–0.088(31)	–	8632	0.1616(29)	1.395(25)	9457	–0.161(13)	–
62	17039	0.35(13)	5.9(21)	10118	0.111(15)	1.13(15)	12805	–0.025(16)	–
63	12976	–0.022(61)	–	9869	–0.154(87)	–	5759	–0.32(55)	–
64	–	–	–	–	–	–	–	–	–
66	14895	0.442(86)	6.6(13)	9745	0.213(9)	2.073(89)	9652	0.166(37)	1.60(36)
67	–	–	–	–	–	–	–	–	–
68	32414	0.191(45)	6.2(15)	47289	1.151(60)	54.4(28)	38773	1.365(68)	52.9(26)
69	–	–	–	–	–	–	–	–	–
70a	38262	0.897(29)	34.3(11)	22038	0.40(12)	8.8(27)	31936	0.41(23)	12.9(74)
70b	33407	1.159(29)	38.72(96)	16255	0.47(25)	7.7(41)	24806	0.090(80)	2.2(20)
71	13660	–0.107(77)	–	11013	0.1869(18)	2.059(19)	9728	–0.24(18)	–
72	35428	0.122(46)	4.3(16)	31768	0.200(11)	6.36(36)	44600	–0.0198(25)	–
73	27890	0.5033(35)	14.038(97)	20101	2.896(23)	58.22(46)	25601	0.438(43)	11.2(11)
76	21667	0.0199(90)	0.43(20)	26169	0.589(83)	15.4(22)	20401	–0.20(23)	–
77a	6874	1.97(26)	13.5(18)	7762	1.616(37)	12.55(29)	5869	0.488(51)	2.86(30)
77b	12460	0.01(12)	0.1(14)	14473	1.676(37)	24.26(53)	26230	0.620(51)	16.3(13)
77c	11596	1.94(12)	22.5(13)	19028	1.586(37)	30.18(70)	7017	0.256(51)	1.80(35)
77d	10347	–0.16(12)	–	4840	0.281(37)	1.36(18)	7758	0.188(61)	1.46(47)
78a	–	–	–	–	–	–	–	–	–
78b	–	–	–	–	–	–	–	–	–
78c	–	–	–	–	–	–	–	–	–
79a	–	–	–	–	–	–	–	–	–
79b	–	–	–	–	–	–	–	–	–
79c	–	–	–	–	–	–	–	–	–
83	19632	1.25(25)	24.5(49)	8203	0.030(59)	0.25(48)	8567	–0.39(23)	–
85a	10647	–	–	11864	–	–	9584	–0.381(25)	–
85b	11961	–	–	16439	0.590(66)	9.7(11)	17858	0.213(25)	3.81(45)
85c	5409	–	–	11796	2.991(66)	35.28(78)	6526	0.080(25)	0.52(16)
117d	–	–	–	–	–	–	–	–	–
117e	–	–	–	–	–	–	–	–	–
118a	1827	–0.60(13)	–	1827	0.31(15)	0.57(27)	1827	0.45(19)	0.81(34)
118b	13681	–0.26(13)	–	29983	–0.50(55)	–	2212	–0.71(23)	–

Table 3 – *continued*

BYF no.	Brackett- γ			H ₂ $v=1\rightarrow 0$			H ₂ $v=2\rightarrow 1$		
	Area	Net Mean	Net Flux	Area	Net Mean	Net Flux	Area	Net Mean	Net Flux
118c	25658	-0.32(13)	–	26030	-0.36(55)	–	15925	-0.06(23)	–
123a	11504	0.148(20)	1.71(23)	8869	–	–	6899	-0.01(10)	–
123b	14545	-0.063(20)	–	7427	–	–	8835	0.15(10)	1.31(89)
123c	12987	–	–	9291	–	–	7017	0.18(10)	1.26(71)
123d	3645	–	–	7117	0.64(19)	4.5(13)	6706	0.29(10)	1.92(68)
126a	56157	85.17(61)	4783(34)	29782	12.8(16)	382(48)	72722	-6.8(26)	–
126b	29695	32.80(27)	973.9(79)	23051	5.4(21)	125(48)	18052	3.2(14)	57(25)
126c	9257	12.06(27)	111.6(25)	20812	2.3(21)	48(44)	11880	4.2(14)	50(16)
126d	17795	1.83(27)	32.6(47)	7117	3.8(21)	27(15)	20649	2.7(14)	55(29)
126e	3645	–	–	7117	3.9(21)	28(15)	18639	3.3(14)	62(26)
128a	25351	19.4(10)	492(26)	8869	75.9(21)	674(19)	11945	2.4(14)	29(16)
128b	31898	30.6(10)	977(33)	35054	8.3(21)	289(73)	20380	0.9(14)	19(28)
208a	32709	-0.48(15)	–	37008	-1.15(17)	–	46299	-0.8(14)	–
208b	23836	-0.08(15)	–	21789	0.12(17)	2.6(38)	23053	–	–

NOTES. The areas of emission are measured in pixels, and the mean values in these areas are in ADUs/pixel (see text). Dashes for certain clumps/filters mean that no emission associated with the clump was discernible in that filter above the immediate surroundings. Uncertainties in brackets are in the last digit of the corresponding value. The net flux values and uncertainties (measured in ADUs) have been divided by 1000 to show significant figures. Notes on individual sources appear below.

7: At edge of field

61b: H₂ $v=1\rightarrow 0$ values uncertain due to proximity to edge

70a: H₂ $v=2\rightarrow 1$ emission was split at $l=286.160$, $b=0.177$

117: At edge of field

118a: Small H₂ $v=1\rightarrow 0$ knot found but no evidence of anything else

123c: The only sign of any emission knots was in H₂ $v=1\rightarrow 0$

3.4 Detailed Correlations

In this section we numerically evaluate the trends apparent above (§3.1). We first examine the mm line ratios. For each of the 60 clumps imaged in the IR, we plot in Figure 3 the $[\text{HCO}^+]/[\text{N}_2\text{H}^+]$ integrated intensity line ratio ηw as a function of $W(\text{HCO}^+)$. Here we see a wide range of η in the clump sample, with measured values $\eta \sim 1.5\text{--}5$ for $W(\text{HCO}^+) \lesssim 9 \text{ K km s}^{-1}$ (corresponding to $W(\text{N}_2\text{H}^+) \sim 1\text{--}3 \text{ K km s}^{-1}$ in this range), and a possibly wider range $\eta \sim 1\text{--}14$ for $W(\text{HCO}^+) \gtrsim 9 \text{ K km s}^{-1}$ (corresponding to $W(\text{N}_2\text{H}^+) \sim 1.5\text{--}15 \text{ K km s}^{-1}$ in this range), although the range at lower $W(\text{HCO}^+)$ may also be somewhat wider due to undetected N_2H^+ in some clumps. There also appears to be a threshold in $W(\text{HCO}^+)$ around 10 K km s^{-1} , below which bright N_2H^+ emission ($W(\text{N}_2\text{H}^+) > 3 \text{ K km s}^{-1}$) is not seen. From the general trends noted above, it already seems clear that clumps with high η are also bright in $\text{Br}\gamma$, while N_2H^+ -bright (i.e., low- η) clumps lie further afield from the $\text{Br}\gamma$ emission.

This disparity between HCO^+ and N_2H^+ becomes more striking when we directly compare the individual mm lines to the IR emission. In Figures 4 and 5 we respectively plot the HCO^+ and N_2H^+ integrated intensities against the total $\text{Br}\gamma$ flux integrated around an area appropriate for each clump, as described in §3.3. We tried both weighted and unweighted least-squares fits to these plots, but found that even a weak inverse-noise weighting tends to produce fits that are strongly dominated by the few points with relatively small errors. Therefore we only give the results of unweighted least-squares fits in the discussion below. Fitting

in this way only the well-measured points (i.e., not including the upper limits for some clumps), we find from Figure 4 that $W(\text{HCO}^+) \propto F(\text{Br}\gamma)^{0.24 \pm 0.04}$. In other words, *the brightness of the HCO^+ emission seems directly tied to the $\text{Br}\gamma$ flux*. In contrast, Figure 5 shows a much weaker correlation between the N_2H^+ emission brightness and the $\text{Br}\gamma$, one that is effectively flat. In other words, *the N_2H^+ emission seems to be independent of the $\text{Br}\gamma$ emission, and may thus better trace gas that is unaffected (or not yet affected) by the presence of massive young stars*. However, we examine a more subtle effect in this plot below (§4.1).

A similar comparison between the mm lines' emission and the H₂ $v=1\rightarrow 0$ nebosity (Figs. 6, 7) shows correlations that are between the above two cases. Thus, while the slope in the power law from Figure 4 is $\sim 5\sigma$ above zero (Pearson's $r^2 = 0.54$), both the $[\text{HCO}^+]\text{--}[\text{H}_2 v=1\rightarrow 0]$ and $[\text{N}_2\text{H}^+]\text{--}[\text{H}_2 v=1\rightarrow 0]$ relations (Figs. 6, 7) seem quite marginal at $\lesssim 3\sigma$ ($r^2 = 0.13$, 0.28 resp.), and the $[\text{N}_2\text{H}^+]\text{--}[\text{Br}\gamma]$ relation (Fig. 5) is very weak ($\sim 2\sigma$, $r^2 = 0.18$). Also, while both HCO^+ and N_2H^+ seem similarly correlated with H₂ $v=1\rightarrow 0$, the HCO^+ emission is systematically brighter than the N_2H^+ by a factor of ~ 3 . Finally, both HCO^+ - and N_2H^+ -bearing clumps exhibit a fairly clear threshold for the detection of H₂ $v=1\rightarrow 0$: one requires $W(\text{HCO}^+) \gtrsim 5 \text{ K km s}^{-1}$ or $W(\text{N}_2\text{H}^+) \gtrsim 2 \text{ K km s}^{-1}$ to reliably detect the $v=1\rightarrow 0$ line. Below this level the $v=1\rightarrow 0$ is sometimes detected, but usually not.

For completeness, we also present in Figures 8 and 9 similar comparisons of the mm line emission with the H₂ $v=2\rightarrow 1$ fluxes. These show similarly marginal trends ($< 3\sigma$) and wider scatter (factors of ~ 3 in y) than Figures 5–7.

A natural question that arises from these plots, espe-

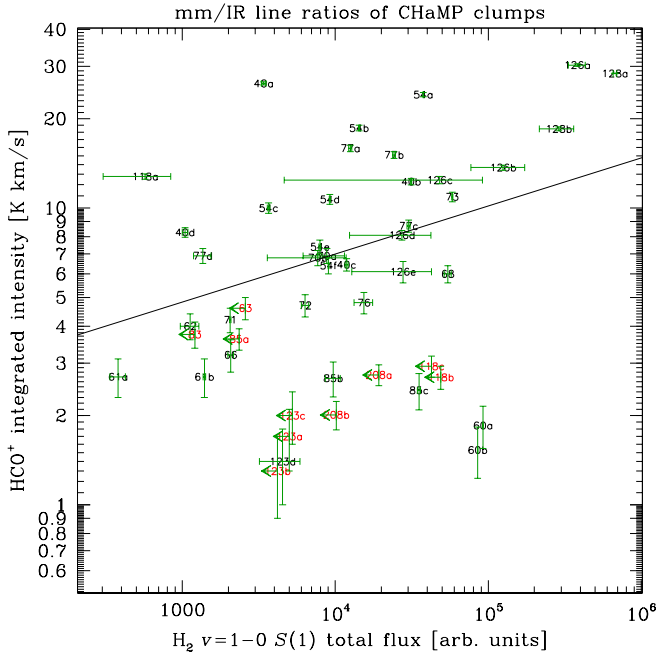


Figure 6. HCO^+ line intensity (on the same ordinate scale as Fig. 4) vs. $\text{H}_2 v=1\rightarrow 0$ integrated flux, labelled by clump number. Other details are as in Fig. 4. Here the unweighted least-squares fit to the well-measured points (black labels) has $m = 0.16 \pm 0.07$, $r^2 = 0.13$, and an rms scatter about this trend of 2.0 in the ordinate (0.30 in $\log y$).

cially Figure 4, is whether the excitation traced by either the $\text{Br}\gamma$ or H_2 emission contributes to the internal turbulence of the molecular clumps? That is, to what extent are the correlations with mm line strengths W determined by the lines' velocity dispersions? To explore this, we show in Figures 10 and 11 a comparison between the HCO^+ and N_2H^+ (resp.) linewidth with the $\text{Br}\gamma$ flux. Clearly if any relationship exists, it shows up only weakly in this sample, with trends that are indistinguishable from scatter plots. An even weaker result is obtained when comparing the mm linewidths to either of the H_2 emission lines (not shown). It must be concluded that the strong trend in Figure 4 is dominated by the brightness of the line emission, rather than due to any contribution from the linewidth. We see this explicitly in Figure 12, with a similar strong correlation ($\sim 4\sigma$) to Figure 4, only with larger errors on the individual points. A plot of N_2H^+ peak brightness vs. $\text{Br}\gamma$ flux (not shown) gives another scatter plot similar to Figure 5.

These relationships are summarised for convenience in Figure 13.

4 DISCUSSION

4.1 Comparison of the mm and IR data

As shown in Paper I, the HCO^+ emission in these massive clumps is almost always optically thin ($\tau \ll 1$), despite being quite bright in some of them. This is true whether we assume a fairly low (10 K) or high (30 K) value for the excitation temperature (T_{ex}) in the HCO^+ line. So, while the exact values for τ in each clump will be somewhat degenerate with

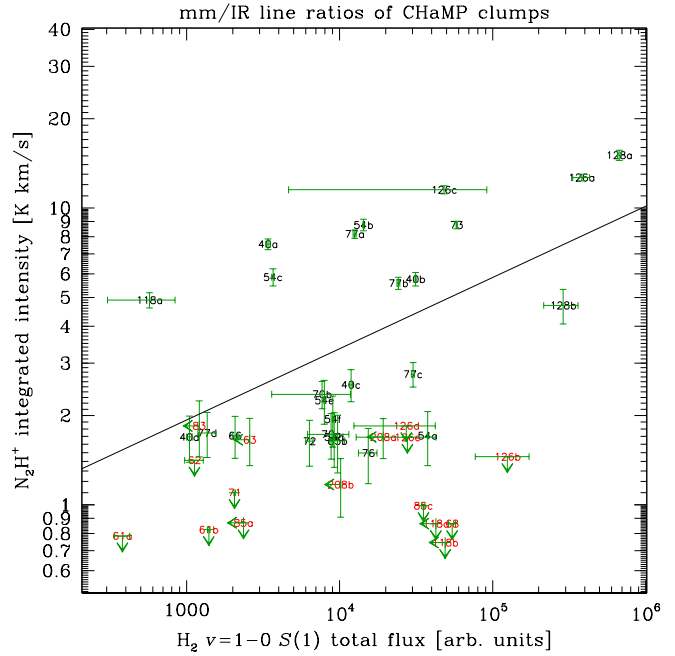


Figure 7. N_2H^+ line intensity (on the same ordinate scale as Fig. 4) vs. $\text{H}_2 v=1\rightarrow 0$ integrated flux, labelled by clump number. Other details are as in Fig. 4. Here the unweighted least-squares fit to the well-measured points (black labels) has $m = 0.24 \pm 0.08$, $r^2 = 0.28$, and an rms scatter about this trend of 2.1 in the ordinate (0.33 in $\log y$).

the assumed T_{ex} , the column density calculated from these lines is quite insensitive to the assumed T_{ex} (e.g., see Fig. 13 in Paper I). Therefore, the integrated intensity $W(\text{HCO}^+)$ should be a reliable indicator of the HCO^+ column density in a molecular clump. (Of course, translating this into a gas or mass column density will depend on the HCO^+ abundance $X(\text{HCO}^+)$, which was discussed in Paper I: we do not revisit that issue here.) This means that *the HCO^+ column density is closely correlated with the $\text{Br}\gamma$ flux from a clump.* In contrast, the N_2H^+ brightness (which to first order, likely also traces its column density) is not obviously correlated to any of the IR emission we have examined here, although there may be a marginally significant relationship with the $\text{H}_2 v=2\rightarrow 1$ flux, and a more subtle correlation with the $\text{Br}\gamma$ which we discuss below. Overall, however, this result seems to support the astrochemical picture of the dependence of HCO^+ and N_2H^+ abundances in dense clumps on the gas temperature (via CO freeze-out) and excitation conditions (discussed further below; see Caselli et al. 2002; Zinchenko et al. 2009). In contrast, the H_2 emission only exhibits weak or marginally significant relationships with either mm line, whereas one might have expected clearer trends than found here. This may also be consistent with the same astrochemical model, if we suppose that, where H_2 emission arises, the destruction of N_2H^+ and production and/or heating of HCO^+ has not progressed as far as in areas emitting $\text{Br}\gamma$.

This hypothesis deserves further examination. The lack of correlation between the mm-lines' velocity dispersions and any of the IR line fluxes suggests that one of the first effects that massive young stars (i.e., those massive enough to ionise significant amounts of gas) have on their natal

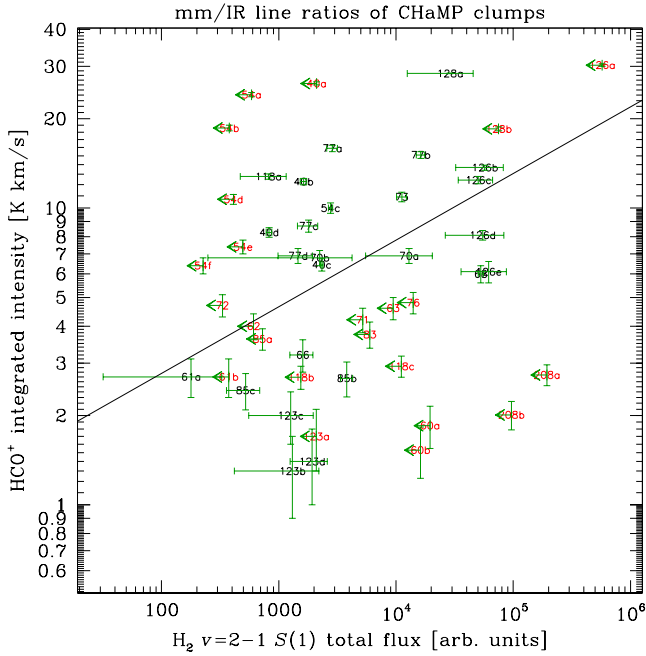


Figure 8. HCO^+ line intensity (on the same ordinate scale as Fig. 4) vs. H_2 $v=2\rightarrow 1$ integrated flux, labelled by clump number. Other details are as in Fig. 4. Here the unweighted least-squares fit to the well-measured points (black labels) has $m = 0.22 \pm 0.09$, $r^2 = 0.22$, and an rms scatter about this trend of 2.1 in the ordinate (0.32 in $\log y$).

molecular environment is one of direct excitation through (photonic) heating, rather than one of mechanical energy injection through winds, shocks, and the like (which would tend to increase the velocity dispersions in the gas). Thus, while we cannot (with these data) confirm the view that turbulent support of these clouds *before massive star formation has commenced* is maintained by low-mass outflow activity (Matzner 2007; Nakamura & Li 2005, 2011), we cannot rule it out either, due to an apparent lack of sensitivity to such activity in these kpc-distant clouds. The lack of correlation of the mm emission (either the lines’ brightness or linewidth) with the “pre-ionised” warm H_2 would simply suggest that gas heated to these intermediate temperatures has not (yet?) spread to significant portions of these massive clumps.

Given the relationships revealed by Figures 3–12, especially Figures 4, 5, and 12. it seems hard to avoid the conclusion that the brightness of the HCO^+ emission (= HCO^+ column density) is being largely driven by the same source(s) that produce the heating and ionisation signified by the $\text{Br}\gamma$ nebulae. In other words, molecular clouds with HCO^+ -enhanced gas seem to signpost the physical interface where massive pre-main sequence stars first begin to heat and drive off their nascent molecular cocoons. Such relationships between HII regions and molecular clouds have, in a gross sense, been seen before (e.g., Blitz, Fich, & Stark 1982), but these have typically been in areas where the dispersal of gas has progressed further, and the young stellar population is less embedded, than in this sample.

Thus, this is the first direct correlation of which we are aware between a standard molecular “dense gas tracer” (HCO^+) and the evolution of the cloud as traced by *ongoing*

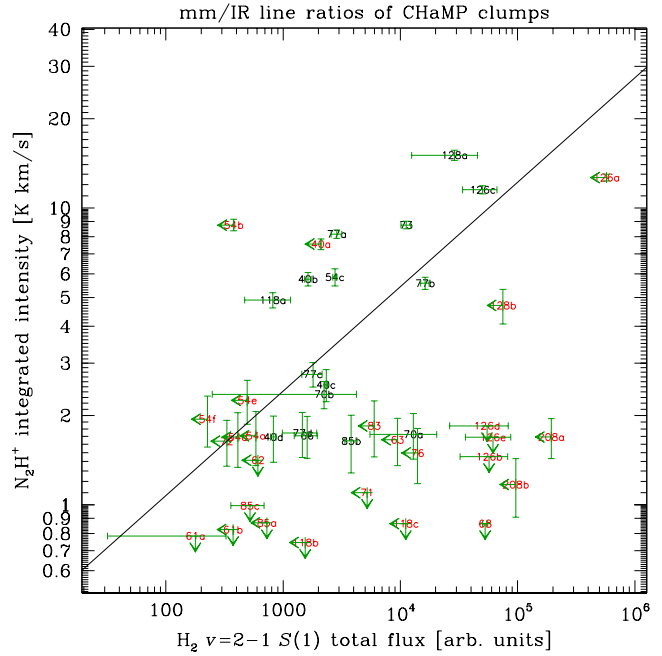


Figure 9. N_2H^+ line intensity (on the same ordinate scale as Fig. 4) vs. H_2 $v=2\rightarrow 1$ integrated flux, labelled by clump number. Other details are as in Fig. 4. Here the unweighted least-squares fit to the well-measured points (black labels) has $m = 0.35 \pm 0.13$, $r^2 = 0.34$, and an rms scatter about this trend of 3.0 in the ordinate (0.47 in $\log y$).

massive star formation activity ($\text{Br}\gamma$ emission). Such a correlation perhaps ought to be expected, but until now there has been little *systematic* information correlating the physical conditions in the dense gas of massive clumps, as traced by their molecular emission alone, with their stellar progeny. By this we mean that, while a good number of IR studies of individual regions, or small collections of regions, have examined (e.g.) H_2 emission in outflows (Caratti o Garatti et al. 2006), there has been little to tie this information to the overall gas properties, or even the gross mm line emission. Similarly, while a number of larger dense molecular gas surveys are now available (e.g., Longmore et al. 2007; Wu et al. 2010; Schlingman et al. 2011), they typically do not relate their data directly to any embedded protostellar content.

What is unexpected is that, as a fairly “standard” dense gas tracer, HCO^+ may turn out to actually trace not mass or density as such, but more likely a combination of gas column density and excitation from embedded massive young stars. On the larger scales of galaxies or GMC complexes in our own Milky Way, “dense gas tracers” are typically thought to represent a fairly homogeneous state of the molecular ISM. Theoretically, this has been challenged by studies such as those of Krumholz & Thompson (2007) or Narayanan et al. (2008), which show that radiative transfer through an entire population of clouds (with a range of properties) must be considered in order to explain (for example) the Kennicutt-Schmidt relationships as traced by these species. Our results suggest that it may be more accurate to think of these tracers as representing a convolution of a larger population of colder, fainter, quiescent clouds with a rarer, brighter cohort that is being actively altered by their newly formed, massive

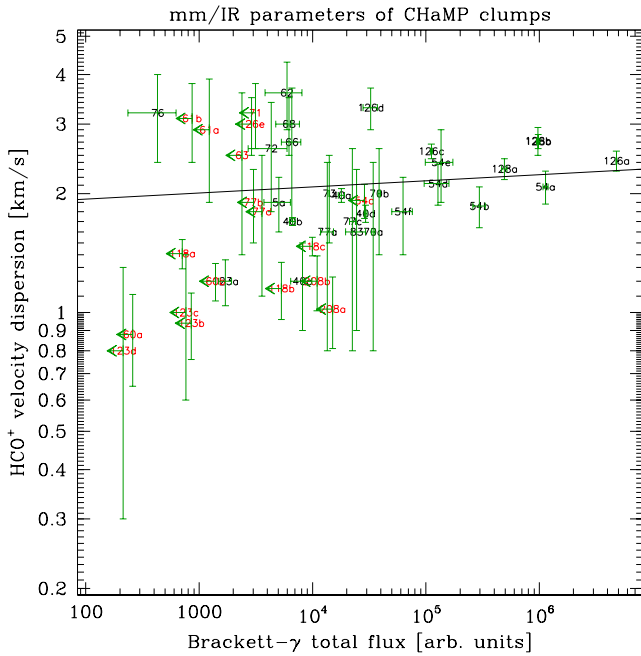


Figure 10. HCO^+ velocity dispersion vs. $\text{Br}\gamma$ integrated flux, labelled by clump number. Other details are as in Fig. 4. Here the unweighted least-squares fit to the well-measured points (black labels and line) has $m = 0.02 \pm 0.03$, $r^2 = 0.01$, and an rms scatter about this trend of 1.3 in the ordinate.

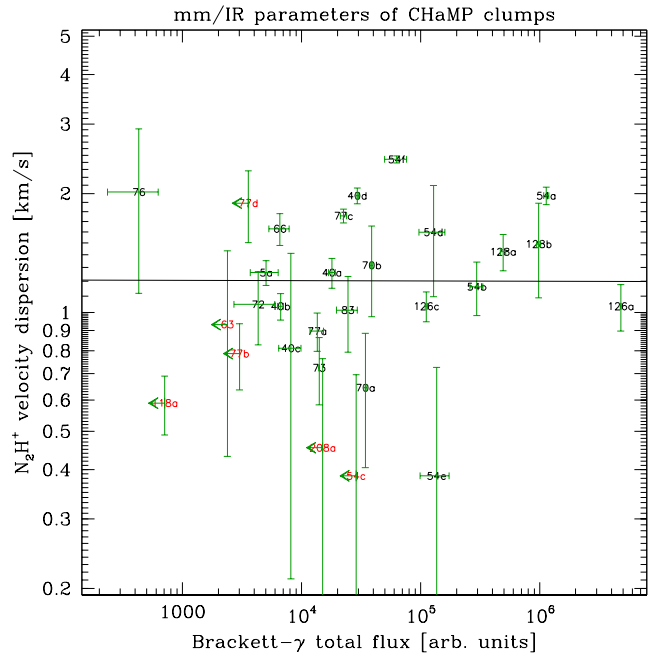


Figure 11. N_2H^+ velocity dispersion vs. $\text{Br}\gamma$ integrated flux, labelled by clump number. Other details are as in Fig. 4. Here the unweighted least-squares fit to the well-measured points (black labels and line) has $m = 0.00 \pm 0.04$, $r^2 = 0.00$, and an rms scatter about this trend of 1.6 in the ordinate.

protostellar products. Such a picture is supported by recent observations of dense-gas tracers on large (~ 100 pc) galactic scales (e.g., in the nuclear bar of Maffei 2; Meier & Turner 2012). The mm line ratio η , in particular, is strongly tied to the presence of star formation and photon-dominated regions (PDRs), in contrast to the ratio of several other pairs of molecular species. Thus, we claim that the case for η being a significant signpost of molecular cloud evolution in the presence of active star formation is now strong, and could be utilised more widely in future studies.

In Paper I we found that massive dense clumps that are HCO^+ -bright ($W > 12 \text{ K km s}^{-1}$) comprise only $\sim 5\%$ of the population of such clumps: 12 of the 15 clumps from Paper I that fall into this category are already included here. Therefore, most of the IR imaging needed to complete this survey will be of the more numerous, fainter population. If the trend in Figure 4 is confirmed in these other clumps, it would tend to strengthen the case for long-lived massive clumps put forward in Paper I, and supported by the results of (e.g.) Narayanan et al. (2008).

What is the physical basis for the significance of η ? N_2H^+ is known to trace better the cold, quiescent, pre-stellar dense gas in low-mass cores (e.g., Caselli et al. 2002) than do other dense-gas tracers like HCO^+ , CS, or HCN. This happens because gas-phase CO is a net destroyer of N_2H^+ , while the HCO^+ abundance is closely tied to the CO. Where CO freezes out onto grains in the coldest parts of molecular clumps and cores, this production of HCO^+ and destruction of N_2H^+ is hindered. Whether this also happens in massive star-forming clumps has hitherto been less clear, although some hint of this has previously emerged (Zinchenko et al. 2009; Schlingman et al. 2011, P. Caselli, in prep.).

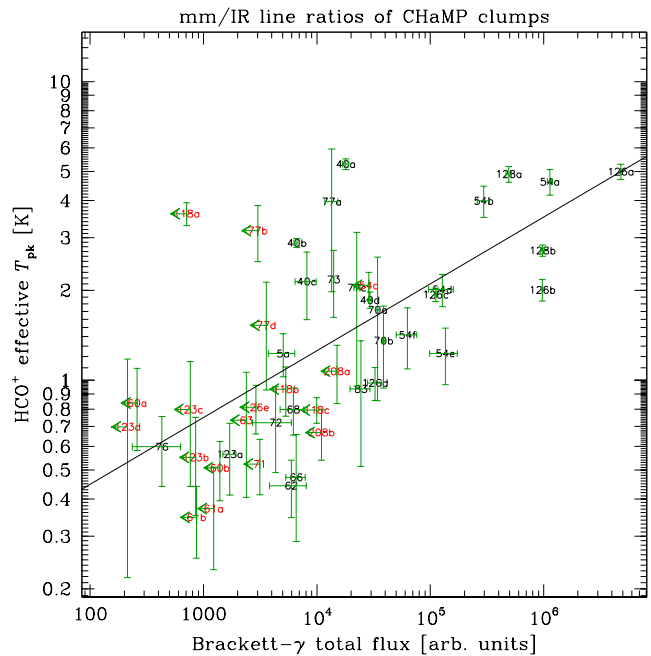


Figure 12. HCO^+ effective T_{pk} vs. $\text{Br}\gamma$ integrated flux, labelled by clump number. Other details are as in Fig. 4. Here the unweighted least-squares fit to the well-measured points (black labels and line) has $m = 0.22 \pm 0.05$, $r^2 = 0.43$, and an rms scatter about this trend of a factor of 1.7 in the ordinate.

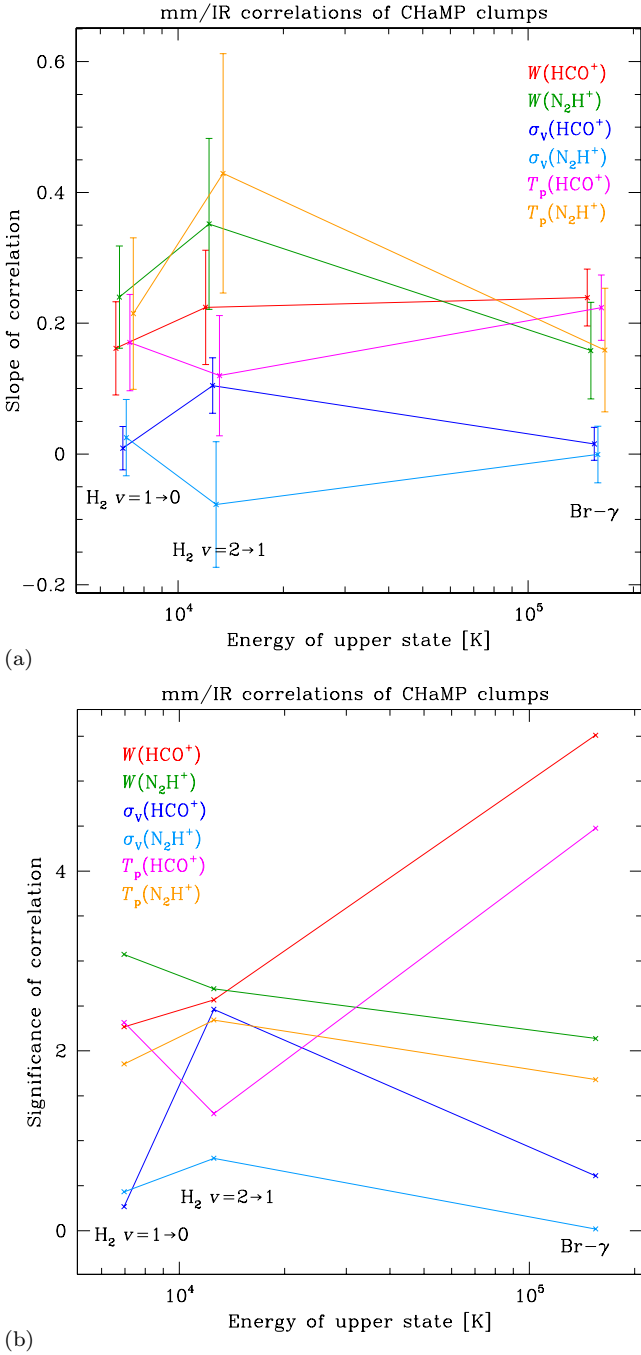


Figure 13. Summary plots of all power-law correlations from Figs. 4–12. (a) Fitted slope of all power laws, with error bars indicating the least-squares uncertainty in the slope. The points are colour-coded for the species (HCO^+ or N_2H^+) and whether the fit was to the integrated intensity, linewidth only, or peak brightness temperature only. For clarity, each point’s abscissa was offset slightly from its nominal value. (b) Significance of the fits shown in panel (a), defined as the slope’s value divided by the uncertainty. One can consider this parameter the “signal-to-noise” of the fitted correlation, and follows well the trend in squared correlation coefficients r^2 (not shown, but given in the caption to each figure). Whether from r^2 or this plot, we see that the most significant correlation among the ones shown is between $W(\text{HCO}^+)$ and $\text{Br}\gamma$ at $>5\sigma$, even though this relation does not have the steepest fitted slope.

Some mm-line studies of dense clumps claim an “evolutionary progression” when only a few examples of the different behaviour of N_2H^+ (or other species) are given. Our larger sample of clumps with both mm-spectroscopic and IR-line data may allow us to establish a more precise version of such a paradigm. We show in Figure 14a a combination of the data from Figures 3–5. While this plot exhibits a fairly weak correlation overall ($\sim 1.3\sigma$), a more subtle but striking trend becomes evident upon closer examination. We now subdivide the clumps into complexes as shown in colour in Figure 14a, and seek a relation within each complex. This is not to claim statistical robustness of any such intra-complex relations, but to test if we can discern a unifying *inter-complex* principle in these relations. Thus, *for clumps within a given complex*, in several instances η appears to be strongly correlated with the $\text{Br}\gamma$ flux: the mean slope of these (admittedly poorly-determined) correlations is $m \sim 0.8$ (cf. $m = 0.26$ from Fig. 4). In other words, without necessarily claiming causality in either direction, the ratio η may possibly be a locally strong function of the ionising flux among the denser clumps within a molecular cloud complex.

Next, we note that in Figure 14a, if granting the possibility of a η – $\text{Br}\gamma$ relation *within* complexes, there seems to be a different normalisation of this relation *between* complexes, spanning ~ 2 orders of magnitude in $\text{Br}\gamma$ flux between the extremes of the BYF 40 and 126/128 complexes. If real, to some extent this might be due to (e.g.) IMF sampling variations, which could strongly affect the EUV and FUV fluxes from a given star cluster of given stellar mass, yet we do not have this information at hand. Nevertheless, we examined several other clump parameters that might hint at a simple physical origin of such a normalisation, such as clump mass, distance, etc. We found that the total bolometric flux from a complex of clumps produces an interesting result, as shown in Figure 14b. This particular normalisation (using data from a companion study to this, of the SEDs of all the CHaMP clumps; Ma et al. 2013) also has the advantage of making Figure 14b distance-independent. With this normalisation, we now fit *all* the clumps within the labelled complexes (i.e., 17 points) with a single least-squares fit. We find the significance of the overall fit to be much higher than those to individual complexes (slope 0.25 ± 0.10 , or 2.4σ), although there may be other parameters such as IMF sampling as above, or 3D projection effects, or the geometry of the ionising source distribution relative to any internal extinction, that contribute to the remaining dispersion. In addition, 6 more normalised points not included in this fit have a small scatter about it.

While perhaps somewhat speculative, we believe this is quite remarkable: it suggests that the relationship between η and $\text{Br}\gamma$ in Figure 14 is much stronger than the relationship in Figure 4 of $\text{Br}\gamma$ to HCO^+ alone. If correct, this would mean that, as the ionising flux rises, the HCO^+ column density is rising *at the same time* as the N_2H^+ column density is falling. Therefore it seems a natural hypothesis to suppose that η and the ionisation state of a clump depend strongly on the *current, local* massive star formation activity among the clumps in question. Together with a similar result from Meier & Turner (2012), we believe our results show, in a fairly direct and robust way, that this indicator (the HCO^+ – N_2H^+ – $\text{Br}\gamma$ relationship) may be a reliable evolutionary signpost in massive star and cluster formation.

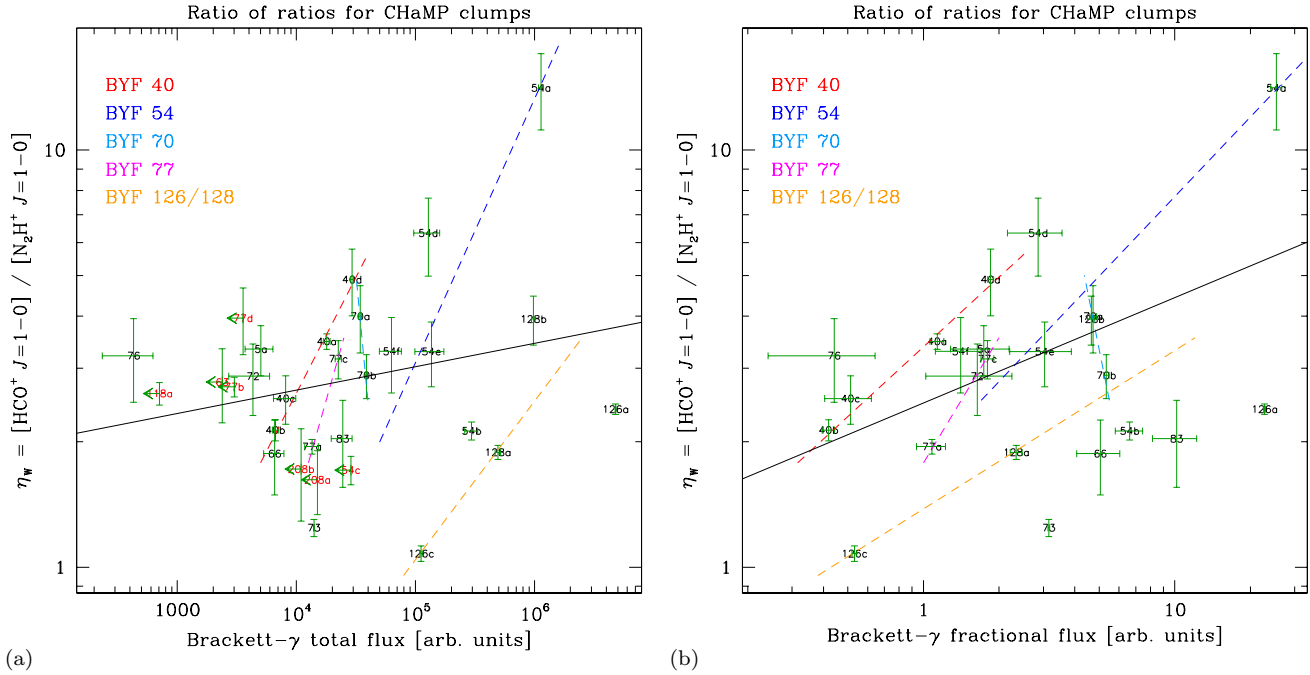


Figure 14. (a) The mm-line ratio η as a function of the Br γ flux, labelled by clump number. Other details are as in Fig. 4. Here the least-squares fit to the well-measured points (black labels and line) has slope $m = 0.06 \pm 0.05$ and correlation coefficient $r^2 = 0.05$, with an rms scatter about this trend of a factor of 1.8 in the ordinate. However, the slopes of fits to individual complexes seem much steeper, as shown in the various colours. (b) Well-measured points from panel a, but now with their Br γ flux normalised to the total bolometric flux of the relevant complex (from Ma et al. 2013). Note the different abscissa scales in these two panels. Here the least-squares fit is only to those 17 points that are part of the labelled complexes. Thus, points for BYF 5a, 66, 72, 73, 76, and 83 were not included in the fit, but nevertheless lie within a factor of ~ 2.5 of this fit, with an rms scatter of 0.27 in $\log y$. The fit itself has $m = 0.25 \pm 0.10$ and $r^2 = 0.28$, with an rms scatter about this trend of only 17% in the ordinate (or 0.067 in $\log y$).

4.2 The IR Lines

In Figure 15 we see that the Br γ and H $_2$ $v=1 \rightarrow 0$ fluxes are marginally well-correlated with each other, which is consistent with the findings above, e.g. that the HCO $^+$ is well-correlated with the Br γ but less so with the H $_2$. A comparison of the Br γ emission with the H $_2$ $v=2 \rightarrow 1$ (not shown) reveals a similar correlation but with a larger uncertainty, again not inconsistent with the mm-IR relationships described earlier, even while it is possible that IMF sampling variations or other factors could also contribute to a large dispersion of NIR line ratios. While a higher flux of emission from excited H $_2$ lines being correlated with a higher flux of Br γ emission is not unexpected, perhaps more illuminating is a direct comparison of the two H $_2$ lines (Fig. 16). Although the correlation between clumps is again marginal, the line ratio itself is diagnostic of different excitation conditions.

For example, Ryder et al. (1998) conducted a detailed study of the H $_2$ line ratio in the reflection nebula Parsamyan 18. They showed that the H $_2$ emission in that source is driven primarily by fluorescence from a single UV-luminous star, coupled with some thermalisation of the $v=1 \rightarrow 0$ line in regions of higher H $_2$ density. Fluorescence alone produces a line ratio $\iota_{21} \sim 0.6$, while thermalisation of the lower- v levels can preferentially enhance the $v=1 \rightarrow 0$ line emission, thus depressing the ι_{21} ratio below its fluorescent value, sometimes significantly ($\iota_{21} < 0.1$). Such small values of ι_{21} can be obtained when the temperature is fairly low ($T_{\text{ex}} \lesssim 2000$ K) and the density high enough to allow the H $_2$ to self-shield

in the presence of a strong UV field ($n > 40G_0 \text{ cm}^{-3}$, where $G_0 = 1$ for the average interstellar radiation field). Since G_0 can exceed 10^4 near massive Young Stellar Objects (YSOs), significant thermalisation of the H $_2$ lines implies the presence of at least some gas at densities $> 10^{5-6}$. The purely thermal ι_{21} ratio will actually depend on the temperature in the H $_2$ gas, e.g. when the H $_2$ excitation temperature $T_{\text{ex}} = 2000$ K, $\iota_{21} = 0.083$, while at $T_{\text{ex}} = 4000$ K, $\iota_{21} = 0.33$ (T. Geballe, 1995)⁶, and at higher temperatures approaches the fluorescent value. Therefore, we see that one requires a high density but low-excitation gas to observe very small ι_{21} ratios in the presence of a strong UV field.

In Figure 16 we see that ι_{21} is consistent (within the uncertainties) with fluorescence in most of our clumps, with a smaller number of sources showing H $_2$ emission that is more thermal in nature. Here fluorescence is the preferred interpretation for $\iota_{21} \sim 0.6$ over high-temperature thermalisation, since the average molecular density in our clumps as determined in Paper I from the HCO $^+$ line data ($n \sim 10^{3-4}$ over the 40'' Mopra beam) is likely too low to afford self-shielding to the H $_2$ when near a massive YSO. But where some clumps have lower ι_{21} , the presence of some higher density molecular gas would seem to be indicated. In each case, the emission morphology tends to match expectations for the physical origin of these line ratios. For example, in

⁶ Quoted by T. Kerr (2004), http://www.jach.hawaii.edu/UKIRT/astronomy/calib/spec_cal/h2_s.html

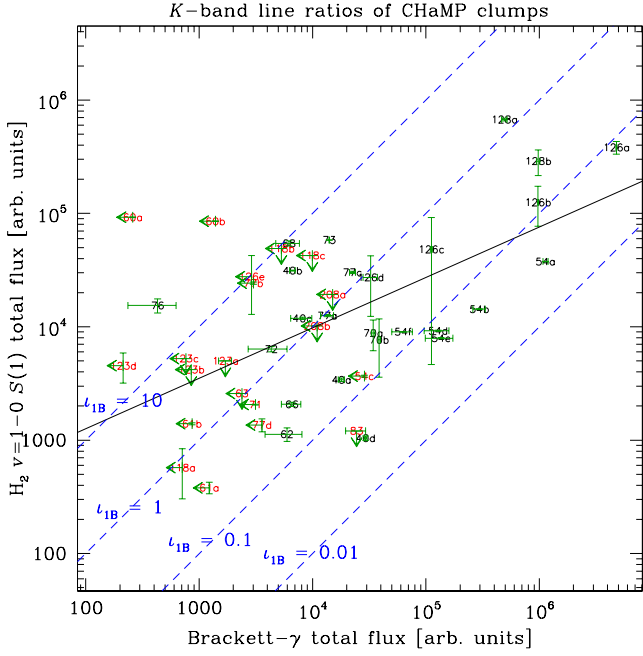


Figure 15. $\text{H}_2 v=1\rightarrow 0$ vs. $\text{Br}\gamma$ integrated fluxes, labelled by clump number. Other details are as in Fig. 4. Here the unweighted least-squares fit to the well-measured points (black labels and line) has slope 0.44 ± 0.13 , with an rms scatter about this trend of a factor of 4.1 in the ordinate. We also show contours of constant line ratio $\iota_{1B} = [v=1\rightarrow 0]/[\text{Br}\gamma]$ in blue.

BYF 70a, 73, or 77b where ι_{21} is close to 0.6, the emission structure is clearly that of HII regions with associated PDRs, and so fluorescence would be expected to drive the H_2 emission. Conversely, in BYF 62 or 72 the $v=2\rightarrow 1$ is hard to detect at all, while the morphology resembles narrow H_2 jets from low-mass protostars which are dominated by thermal emission from shocks. Curiously, while the BYF 54 clumps (see Fig. 2) show very strong $\text{Br}\gamma$ and $\text{H}_2 v=1\rightarrow 0$ emission, the $v=2\rightarrow 1$ emission is virtually non-existent and $\iota_{21} \ll 1$, implying that the $v=1\rightarrow 0$ nebulosity we see is dominated by thermal emission at low temperatures (i.e., ~ 1000 K), despite their projected proximity to what seem like PDRs adjacent to HII regions. Therefore, it may be that this complex has, e.g., unusually strong wind shocks exciting the H_2 emission, instead of the (apparently) more usual fluorescence, and may be worth deeper investigation on this basis.

Finally, we reiterate that the calibration dispersion could not create a spurious correlation of the form in Figure 4; indeed it would only weaken the true correlation. In particular, Figure 14 would be unaffected by any variations in transparency, as all complexes within a clump were observed simultaneously. Similarly in Figures 15 and 16, since the $\text{Br}\gamma$ and both H_2 lines were nearly always observed within $\sim 20''$ of each other, it is likely that each experienced similar atmospheric conditions, changes in which would only move any clump parallel to the blue dashed lines, but not otherwise smear out any underlying correlation.

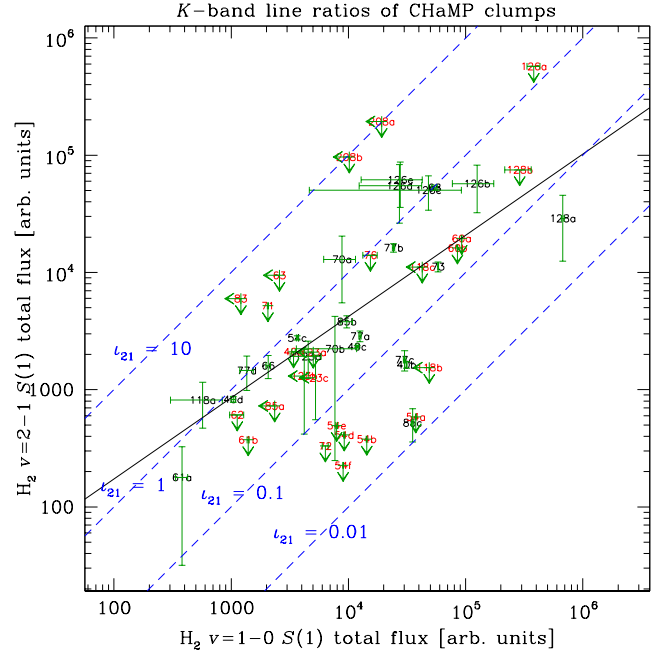


Figure 16. $\text{H}_2 v=2\rightarrow 1$ vs. $v=1\rightarrow 0$ integrated fluxes, labelled by clump number. Other details are as in Fig. 4. Here the unweighted least-squares fit to the well-measured points (black labels and line) has slope 0.69 ± 0.15 , with an rms scatter about this trend of a factor of 4.0 in the ordinate. We also show contours of constant line ratio $\iota_{21} = [v=2\rightarrow 1]/[v=1\rightarrow 0]$ in blue.

5 CONCLUSIONS

We have presented new results of mm-wave and near-IR emission-line imaging of 60 massive, dense, star-forming molecular clumps, the first $\sim 20\%$ of the CHaMP sample (Paper I). From these, we see the first systematic variations in line ratios with clump evolutionary state. Our findings include the following.

1. Among the clumps showing bright molecular emission in HCO^+ and N_2H^+ , there is a wide variation in the intensity ratio η of these lines, from ~ 1 –14. Among the fainter clumps, η is somewhat more uniform, ~ 2 –5.

2. The HCO^+ intensity of the clumps is strongly correlated with the $\text{Br}\gamma$ integrated flux associated with the clump, while the N_2H^+ intensity appears relatively uncorrelated with the $\text{Br}\gamma$ emission, when measured across all clumps. There are also weaker correlations between either molecular species and the associated H_2 IR emission lines. The $W(\text{HCO}^+)$ - $\text{Br}\gamma$ relation arises mostly in the line brightness, rather than the linewidth, suggesting that the dominant effect of the energy output of massive YSOs on the clump gas is radiative, rather than mechanical. This is consistent with the fluorescent interpretation for the H_2 line emission, below.

3. The mm-line ratio $\eta = [\text{HCO}^+]/[\text{N}_2\text{H}^+]$ is even more strongly correlated with bright $\text{Br}\gamma$ emission among clumps *within* a given molecular complex, and is at least partly normalised *between* complexes by the total bolometric luminosity of the complex. This situation occurs in the minority of all our clumps, i.e. those with a significant nearby UV field from embedded massive YSOs. The majority of our

clumps show only a mild, apparently random variation in $\eta \sim 2-5$.

4. This suggests a common trend among massive dense clumps in the presence of active massive star and star cluster formation. Before significant massive star formation has occurred in a clump, the $\text{HCO}^+/\text{N}_2\text{H}^+$ column density ratio η is constant to within a factor of ~ 2 . As the ionising flux impinging upon a clump rises, the HCO^+ column density rises while the N_2H^+ column density simultaneously falls.

5. We propose that the η -Br γ relation is a useful new diagnostic of the progress in a massive molecular clump towards the formation of massive clusters with stars of sufficient luminosity to ionise and potentially disperse the clump.

6. In most cases, the H_2 emission is consistent with fluorescent excitation in PDRs near HII regions, and the emission morphology often conforms to this origin. In a few cases, the H_2 emission seems mostly thermally excited, and again the morphology in such instances often resembles that from protostellar jets driving shocks into the surrounding gas. BYF 54 seems to be a counterexample to both these groups, exhibiting thermal H_2 line ratios in the presence of a strong UV field.

These and other results suggest that the $\text{HCO}^+/\text{N}_2\text{H}^+$ intensity ratio η , together with the Br γ flux, may provide useful signposts of massive star formation, and allow us to tie observations more closely to certain theoretical models of the evolution of massive, dense molecular clumps, contributing to a more complete picture of the formation of massive stars and star clusters.

ACKNOWLEDGMENTS

We thank the staff members of the ATNF and AAO for their support of the observations. PJB gratefully acknowledges support through NSF grant AST-0645412 to JCT at the University of Florida, a Professional Development Leave award in 2011 from the University of Florida, and receipt of an AAO Distinguished Visitorship in 2011. SNO and LEA were partially supported by an REU supplement to JCT's NSF grant. We also thank the referee for helpful suggestions and comments which led to several improvements in the paper.

FACILITIES: Mopra (MOPS), AAT (IRIS2)

REFERENCES

- Aguirre, J. E., et al. 2011, ApJS, 192, 4
 Barnes, P. J., Yonekura, Y., Ryder, S. D., Hopkins, A. M., Miyamoto, Y., Furukawa, N., & Fukui, Y. 2010, MNRAS, 402, 73
 Barnes, P. J., et al. 2011, ApJS, 196, 12 (Paper I)
 Benjamin, R. A., et al. 2003, PASP, 115, 953
 Beuther, H., Churchwell, E. B., McKee, C. F., & Tan, J. C. 2007, in Protostars and Planets V, B. Reipurth, D. Jewitt, and K. Keil (eds.) (Tucson: U. of Arizona Press), p165
 Blitz L, Fich M, & Stark A A 1982, ApJS, 49, 183
 Caratti o Garatti A., Giannini T., Nisini B., & Lorenzetti D. 2006, A&A, 449, 1077–1088
 Caselli, P., Walmsley, C. M., Zucconi, A., Tafalla, M., Dore, L., & Myers, P. C. 2002, ApJ, 565, 344
 Cavanagh, B., Hirst, P., Jenness, T., Economou, F., Currie, M. J., Todd, S., & Ryder, S. D. 2003, in ASP Conf. Ser., Astronomical Data Analysis Software and Systems XII, eds. H. E.

- Payne, R. I. Jedrzejewski, & R. N. Hook (San Francisco: ASP), 295, 237
 Fröbrich, D., and 32 co-authors 2011, MNRAS, 413, 480
 Higuchi, A. E., Kurono, Y., Saito, M., & Kawabe, R. 2009, ApJ, 705, 468
 Krumholz, M. R. & Thompson, T. A. 2007, ApJ, 669, 289
 Lada, C. J., & Lada, E. A. 2003, ARA&A, 41, 57
 Longmore, S. N., Burton, M. G., Barnes, P. J., Wong, T., Purcell, C. R., & Ott, J. 2007, MNRAS, 379, 535
 Ma, B., Tan, J.C., & Barnes, P.J. 2013, ApJ, submitted (arXiv: 1211.6492)
 Matzner, C. D. 2007, ApJ, 659, 1394
 Meier, D. S. & Turner, J. L. 2012, ApJ, 755, 104
 Molinari, S. et al. 2010, A&A, 518, 100
 Nakamura, F. & Li, Z-Y. 2005 ApJ, 631, 411
 Nakamura, F. & Li, Z-Y. 2011 ApJ, 740, 36
 Narayanan, D., Cox, T. J., Shirley, Y., Davé, R., Hernquist, L., & Walker, C. K. 2008, ApJ, 684, 996
 Pirogov, L., Zinchenko, I., Caselli, P., & Johansson, L. E. B. 2007, A&A, 461, 523
 Ryder, S. D., Allen, L. E., Burton, M. G., Ashley, M. C. B., & Storey, J. W. V. 1998, MNRAS, 294, 338
 Sault, R. J., Teuben, P. J., & Wright, M. C. H., 1995. in “Astronomical Data Analysis Software and Systems IV”, eds. R. Shaw, H. E. Payne, J. J. E. Hayes, ASP Conference Series, 77, 433
 Schlingman, W. M., et al. 2011, ApJS, 195, 14
 Tinney, C. G., et al. 2004, Proc. SPIE, 5492, 998
 Wu, J., Evans, N. J. II, Shirley, Y. L., & Knez, C. 2010, ApJS, 188, 313
 Yonekura, Y., Asayama, S., Kimura, K., Ogawa, H., Kanai, Y., Yamaguchi, N., Barnes, P. J., & Fukui, Y. 2005, ApJ, 634, 476
 Zinchenko, S., Caselli, P., & Pirogov, L. 2009, MNRAS, 395, 2234

SUPPORTING INFORMATION

Additional Supporting Information may be found in the on-line version of this article:

Appendix A: Narrow-band NIR Images.

APPENDIX A: NARROW-BAND NEAR-INFRARED IMAGES

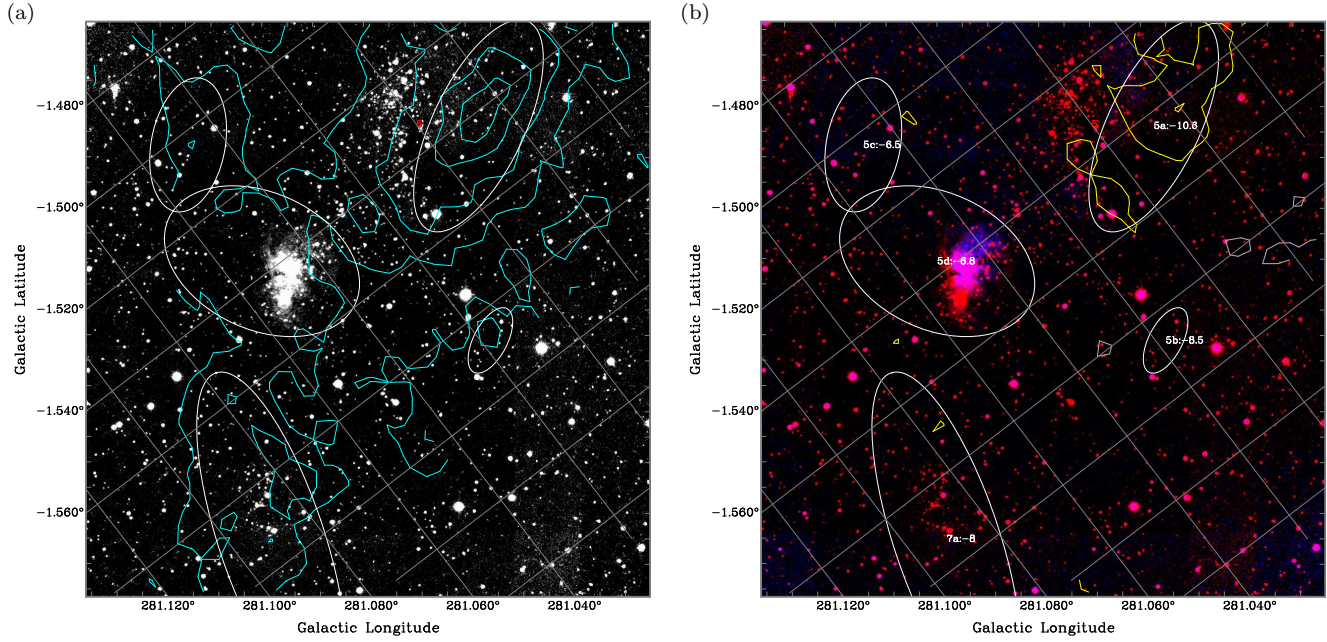


Figure A1. (a) *K*-band line-free continuum image of BYF 5 (part of Region 1 from Paper I) on a linear brightness scale. Contours are overlaid from Mopra HCO^+ integrated intensity (cyan levels at 4, 8, 12, and 16 times the rms level of $0.318 \text{ K km s}^{-1}$), while the white ellipses represent gaussian fits to the HCO^+ emission. (b) Colour-composite image of continuum-subtracted $\text{Br}\gamma$ (blue) with the same image as in (a) (red) on a linear brightness scale. (Poor weather prevented us from obtaining the corresponding images for this field in the other filters.) Overlaid here are contours of Mopra N_2H^+ integrated intensity (grey levels at -3 and yellow at 3 times the rms of $0.274 \text{ K km s}^{-1}$) with the same ellipses as in (a). At a distance of 3.2 kpc, the scale is $40'' = 0.621 \text{ pc}$ or $1 \text{ pc} = 0^\circ.0229 = 64''.5$. In this and subsequent figures, images not otherwise indicated are from observations in 2011 with shorter integration times. Images from deeper 2006–07 data are so noted.

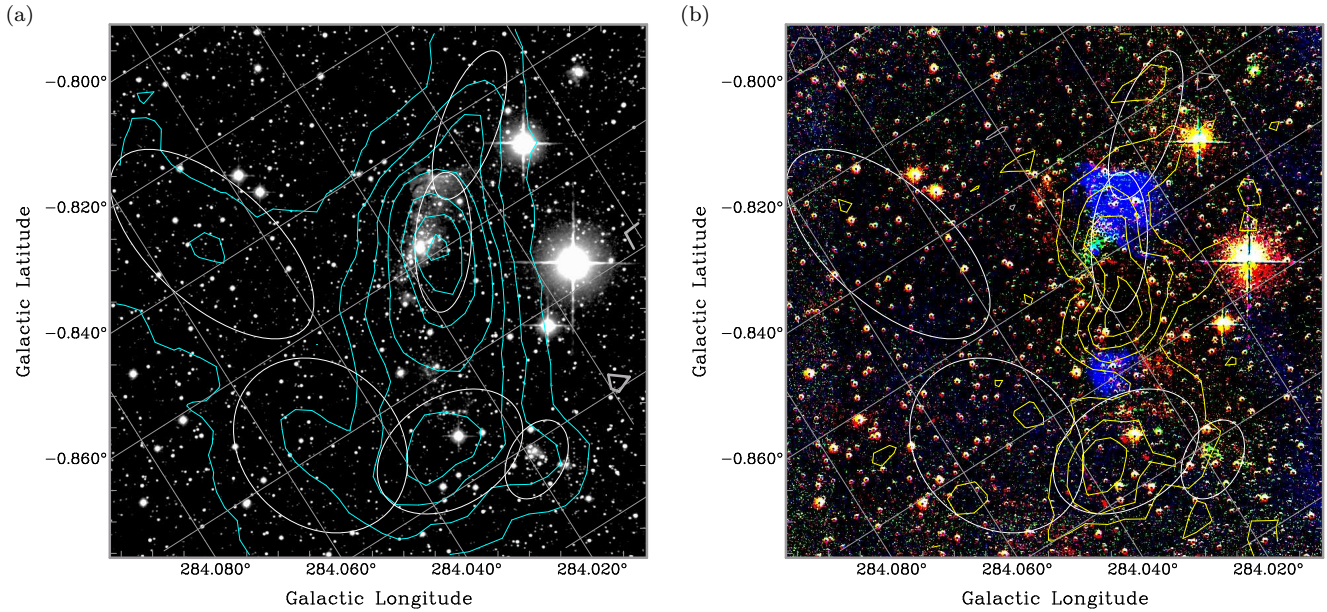


Figure A2. Same as Fig. 2, but for BYF 40 (part of Region 6 from Paper I) using more sensitive 2006 data. (a) *K*-band line-free continuum image with HCO^+ contours (heavy grey at 0, cyan at 8, 16, 24, 32, 48, 64, and 80 times the rms level of $0.312 \text{ K km s}^{-1}$). (b) RGB-pseudo-colour image of the continuum-subtracted *K*-band spectral lines N_2H^+ contours (grey at -2.5 , yellow at 2.5, 5, 7.5, and 10 times the rms of $0.588 \text{ K km s}^{-1}$). White ellipses show gaussian fits to the HCO^+ emission in both panels. At a distance of 2.5 kpc, the scale is $40'' = 0.485 \text{ pc}$ or $1 \text{ pc} = 0^\circ.0229 = 82''.5$.

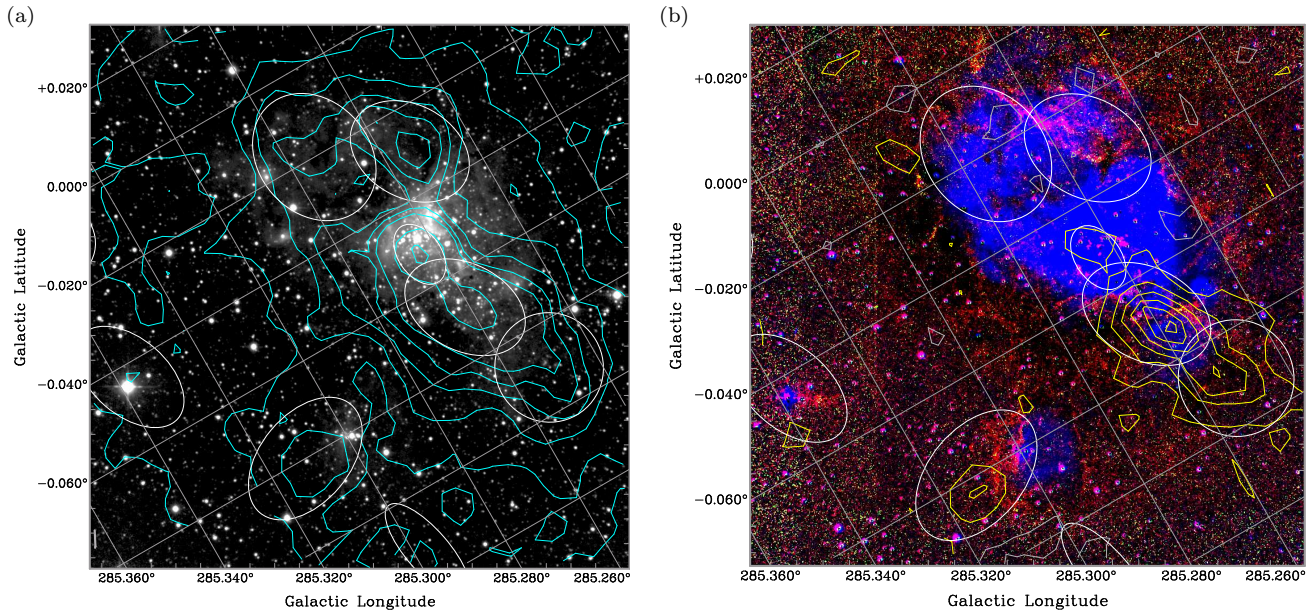


Figure A3. Same as Fig. 2, but for BYF 54 (part of Region 8 from Paper I) using more sensitive 2006 data. (a) *K*-band line-free continuum image with HCO^+ contours (heavy grey at 0, cyan at 4, 8, 12, 16, 20, 24, 40, and 56 times the rms level of $0.401 \text{ K km s}^{-1}$). (b) RGB-pseudo-colour image of the continuum-subtracted *K*-band spectral lines with N_2H^+ contours (grey at -2 , yellow at 2, 4, 6, 8, 10, and 12 times the rms level of $0.603 \text{ K km s}^{-1}$). White ellipses show gaussian fits to the HCO^+ emission in both panels. At a distance of 2.5 kpc, the scale is $40'' = 0.485 \text{ pc}$ or $1 \text{ pc} = 0^\circ 02' 29'' = 82''.5$.

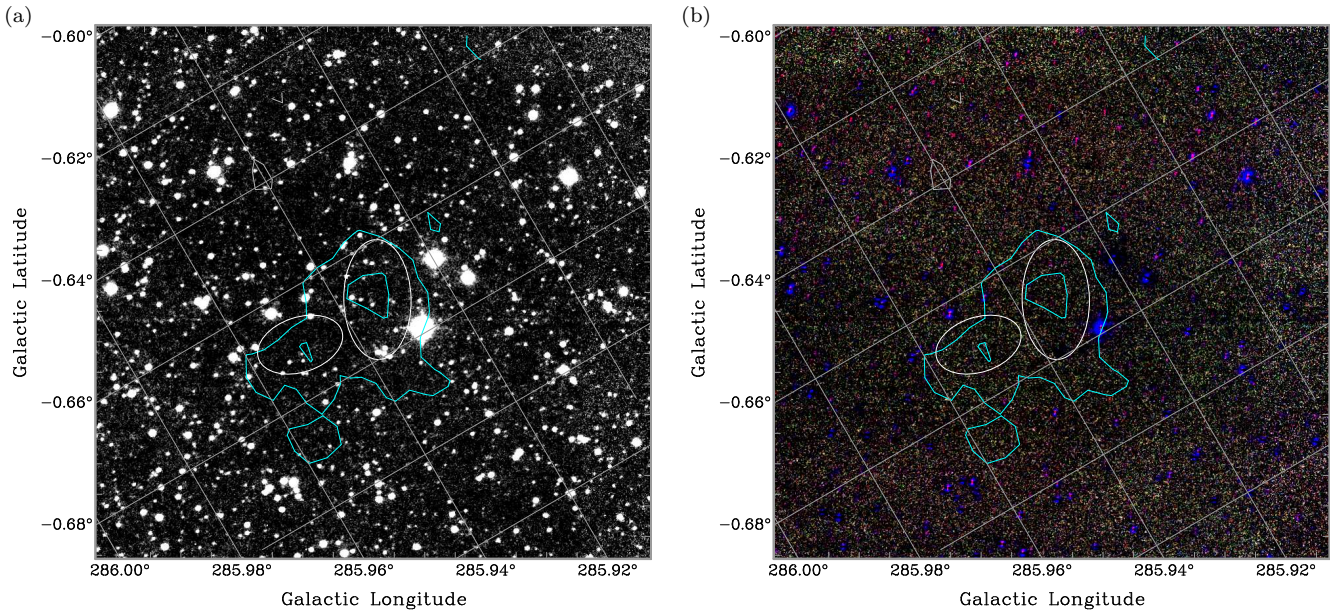


Figure A4. Same as Fig. 2, but for BYF 60 (part of Region 9 from Paper I). (a) *K*-band line-free continuum image with HCO^+ contours (grey at -2.5 and cyan at 2.5 and 5 times the rms level of $0.295 \text{ K km s}^{-1}$). (b) RGB-pseudo-colour image of the continuum-subtracted *K*-band spectral lines with the same contours as in (a) (N_2H^+ was not mapped in this field). White ellipses show gaussian fits to the HCO^+ emission in both panels. At a distance of 5.3 kpc, the scale is $40'' = 1.03 \text{ pc}$ or $1 \text{ pc} = 0^\circ 01' 08'' = 38''.9$.

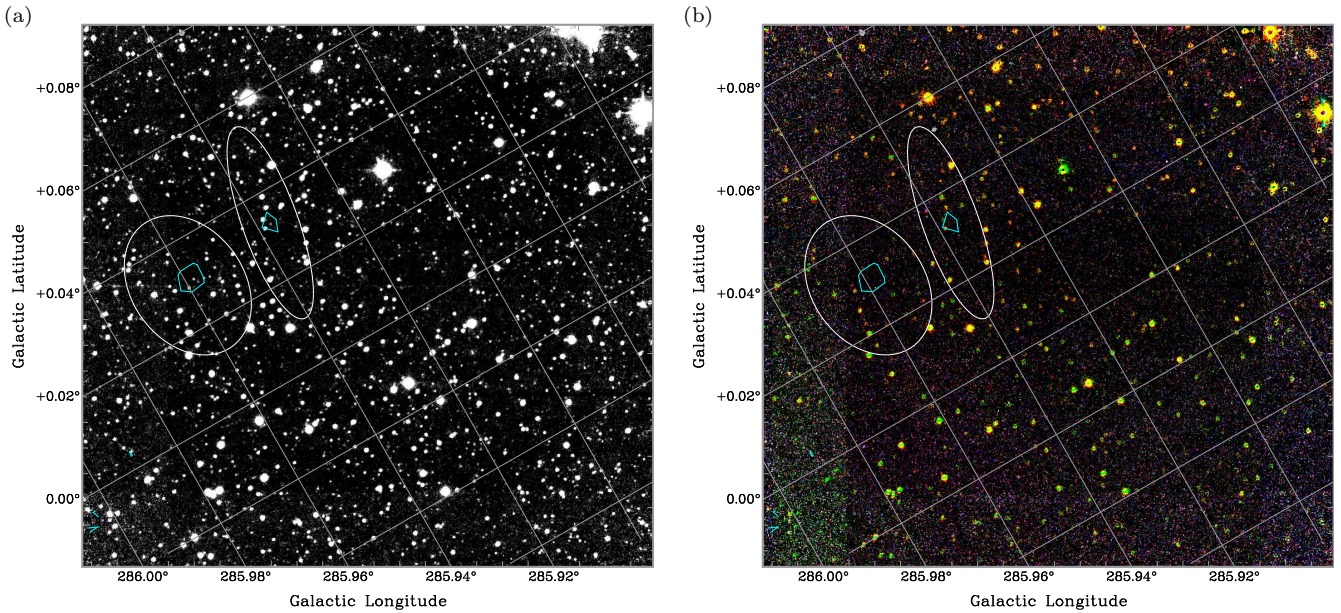


Figure A5. Same as Fig. 2, but for BYF 61 (part of Region 9 from Paper I, see Fig. 1). (a) *K*-band line-free continuum image with both HCO⁺ contours (heavy grey at 0 and cyan at 6, 10, and 14 times the rms level of 0.404 K km s⁻¹) and N₂H⁺ contours (grey at -3 and yellow at 3 times the rms level of 0.253 K km s⁻¹). (b) RGB-pseudo-colour image of the continuum-subtracted *K*-band spectral lines with the same contours as in (a). White ellipses show gaussian fits to the HCO⁺ emission in both panels. At a distance of 2.5 kpc, the scale is 40'' = 0.485 pc or 1 pc = 0°0229 = 82''5.

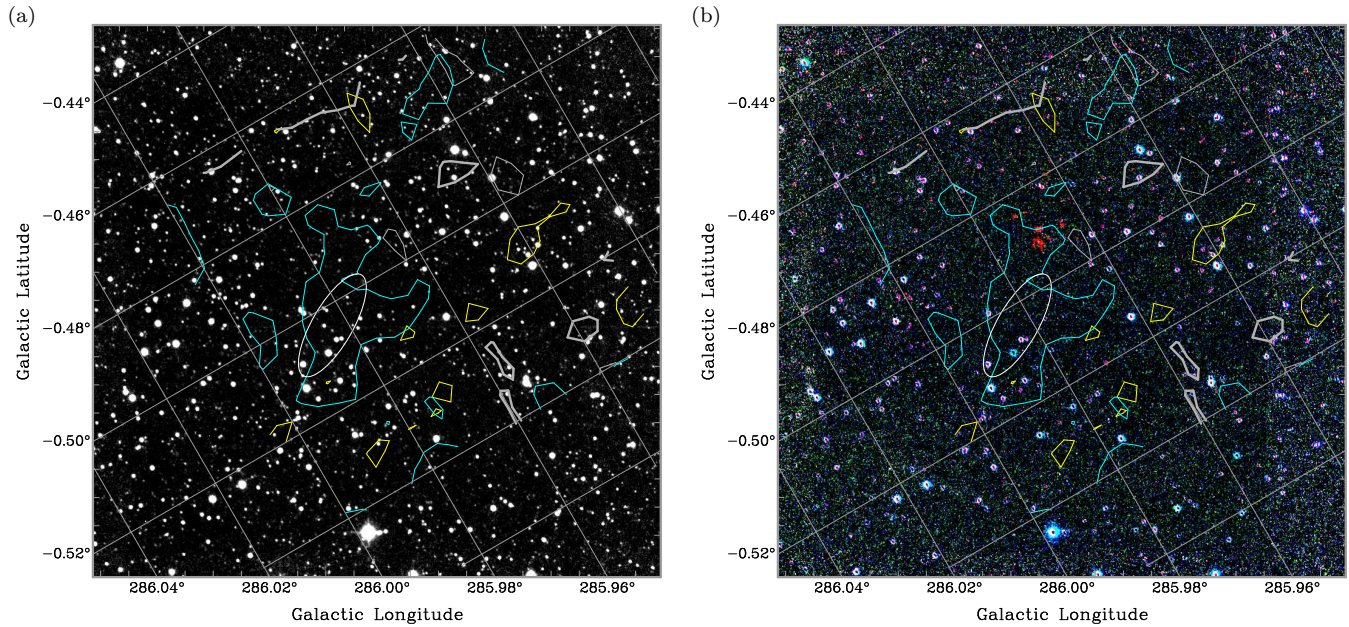


Figure A6. Same as Fig. 2, but for BYF 62 (part of Region 9 from Paper I, see Fig. 1). (a) *K*-band line-free continuum image with both HCO⁺ contours (heavy grey at 0 and cyan at 6, 10, and 14 times the rms level of 0.404 K km s⁻¹) and N₂H⁺ contours (grey at -3 and yellow at 3 times the rms level of 0.253 K km s⁻¹). (b) RGB-pseudo-colour image of the continuum-subtracted *K*-band spectral lines with the same contours as in (a). The white ellipse shows a gaussian fit to the HCO⁺ emission in both panels. At a distance of 2.5 kpc, the scale is 40'' = 0.485 pc or 1 pc = 0°0229 = 82''5.

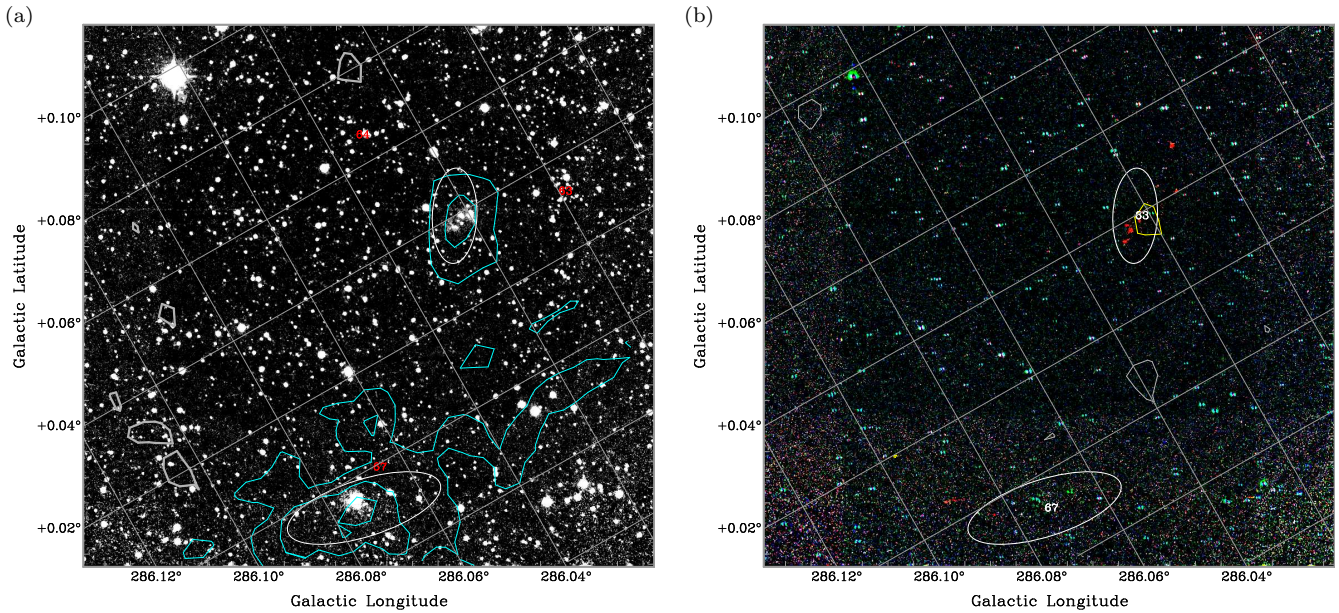


Figure A7. Same as Fig. 2, but for BYF 63 and 67 (part of Region 9 from Paper I, see Fig. 1). (a) K -band line-free continuum image with HCO^+ contours (heavy grey at 0 and cyan at 6, 10, and 14 times the rms level of $0.404 \text{ K km s}^{-1}$). (b) RGB-pseudo-colour image of the continuum-subtracted K -band spectral lines with N_2H^+ contours (grey at -3 and yellow at 3 times the rms level of $0.253 \text{ K km s}^{-1}$). White ellipses show gaussian fits to the HCO^+ emission in both panels. At a distance of 2.5 kpc, the scale is $40'' = 0.485 \text{ pc}$ or $1 \text{ pc} = 0^{\circ}0229 = 82''5$.

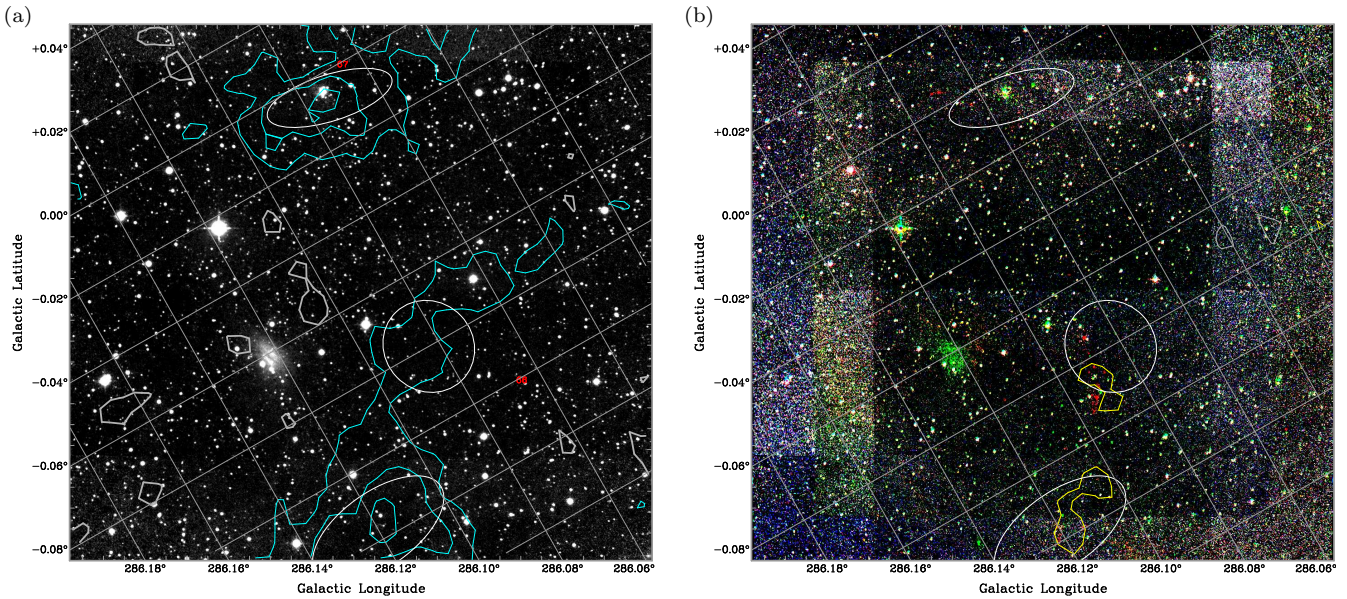


Figure A8. Same as Fig. 2, but for BYF 67, 66, and 69 (part of Region 9 from Paper I, see Fig. 1). (a) K -band line-free continuum image with HCO^+ contours (heavy grey at 0 and cyan at 6, 10, and 14 times the rms level of $0.404 \text{ K km s}^{-1}$). (b) RGB-pseudo-colour image of the continuum-subtracted K -band spectral lines with N_2H^+ contours (grey at -3 and yellow at 3 times the rms level of $0.253 \text{ K km s}^{-1}$). White ellipses show gaussian fits to the HCO^+ emission in both panels. At a distance of 2.5 kpc, the scale is $40'' = 0.485 \text{ pc}$ or $1 \text{ pc} = 0^{\circ}0229 = 82''5$. Note the \sim arcmin-sized background galaxy at $l = 286^{\circ}12$, $b = -0^{\circ}16$.

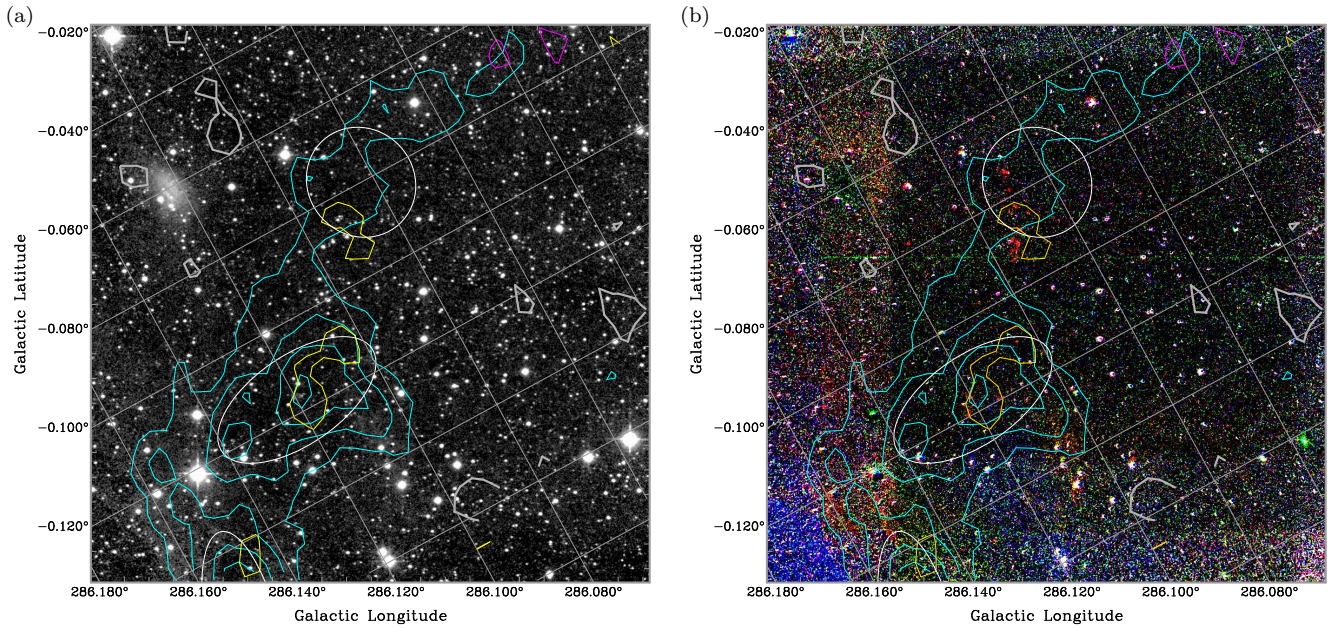


Figure A9. Same as Fig. 2, but for BYF 66 and 69 (part of Region 9 from Paper I, see Fig. 1) using more sensitive 2007 data. (a) K -band line-free continuum image with both HCO^+ contours (heavy grey at 0, cyan at 6, 9, 12, and 15 times the rms level of $0.404 \text{ K km s}^{-1}$) and N_2H^+ contours (yellow at -3 , gold at $+3$ times the rms level of $0.253 \text{ K km s}^{-1}$). (b) RGB-pseudo-colour image of the continuum-subtracted K -band spectral lines with the same contours as in (a). White ellipses show gaussian fits to the HCO^+ emission in both panels. At a distance of 2.5 kpc , the scale is $40'' = 0.485 \text{ pc}$ or $1 \text{ pc} = 0^{\circ}0229 = 82''.5$. Note the \sim arcmin-sized background galaxy at $l = 286^{\circ}12$, $b = -0^{\circ}16$.

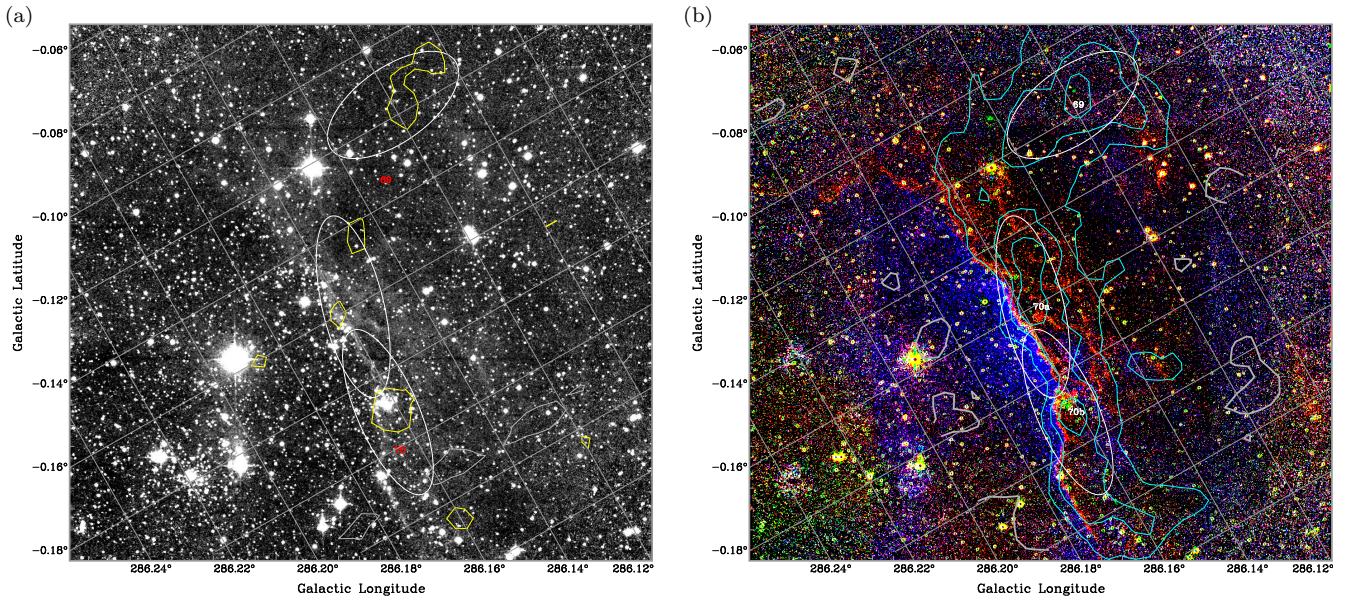


Figure A10. Same as Fig. 2, but for BYF 69 and 70 (part of NGC 3324 and Region 9 from Paper I, see Fig. 1). (a) K -band line-free continuum image with N_2H^+ contours (grey at -3 and yellow at 3 times the rms level of $0.253 \text{ K km s}^{-1}$). (b) RGB-pseudo-colour image of the continuum-subtracted K -band spectral lines with HCO^+ contours (heavy grey at 0 and cyan at 6, 10, and 14 times the rms level of $0.404 \text{ K km s}^{-1}$). White ellipses show gaussian fits to the HCO^+ emission in both panels. At a distance of 2.5 kpc , the scale is $40'' = 0.485 \text{ pc}$ or $1 \text{ pc} = 0^{\circ}0229 = 82''.5$.

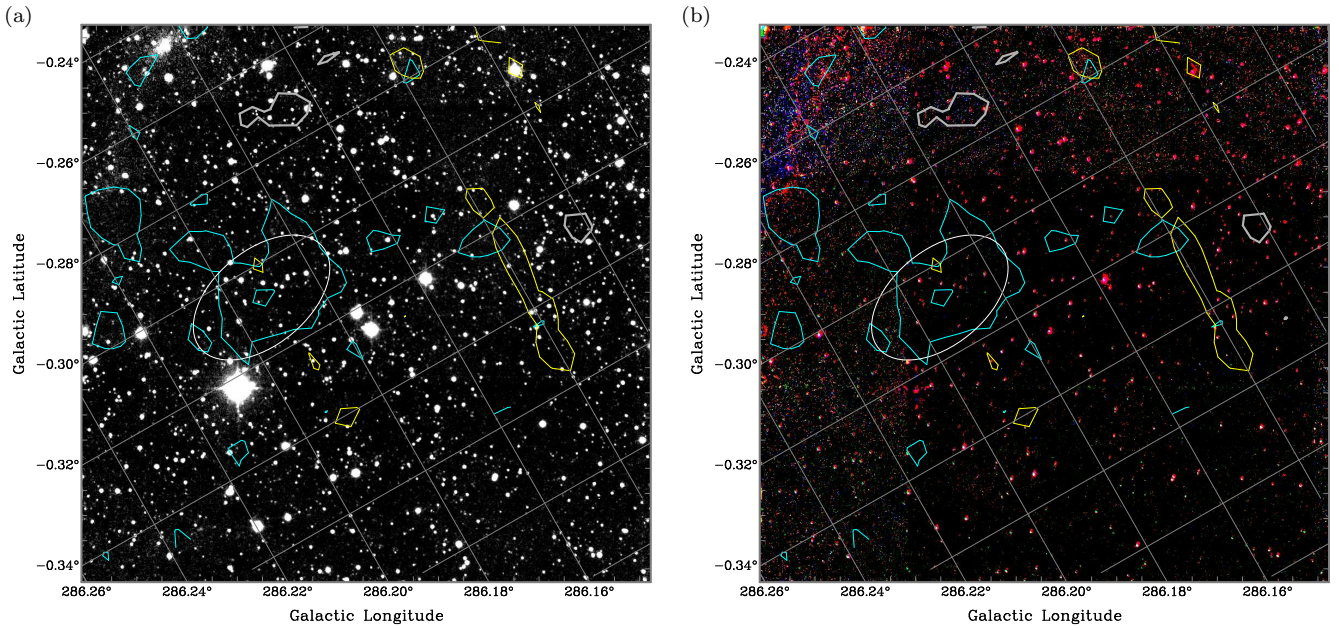


Figure A11. Same as Fig. 2, but for BYF 71 (part of Region 9 from Paper I, see Fig. 1). (a) K -band line-free continuum image with HCO^+ contours (heavy grey at 0, cyan at 6 and 10 times the rms level of $0.404 \text{ K km s}^{-1}$) and N_2H^+ contours (grey at -3 and yellow at 3 times the rms level of $0.253 \text{ K km s}^{-1}$). (b) RGB-pseudo-colour image of the continuum-subtracted K -band spectral lines with the same contours as in (a). The white ellipse shows a gaussian fit to the HCO^+ emission in both panels. At a distance of 2.5 kpc, the scale is $40'' = 0.485 \text{ pc}$ or $1 \text{ pc} = 0^\circ.0229 = 82''.5$.

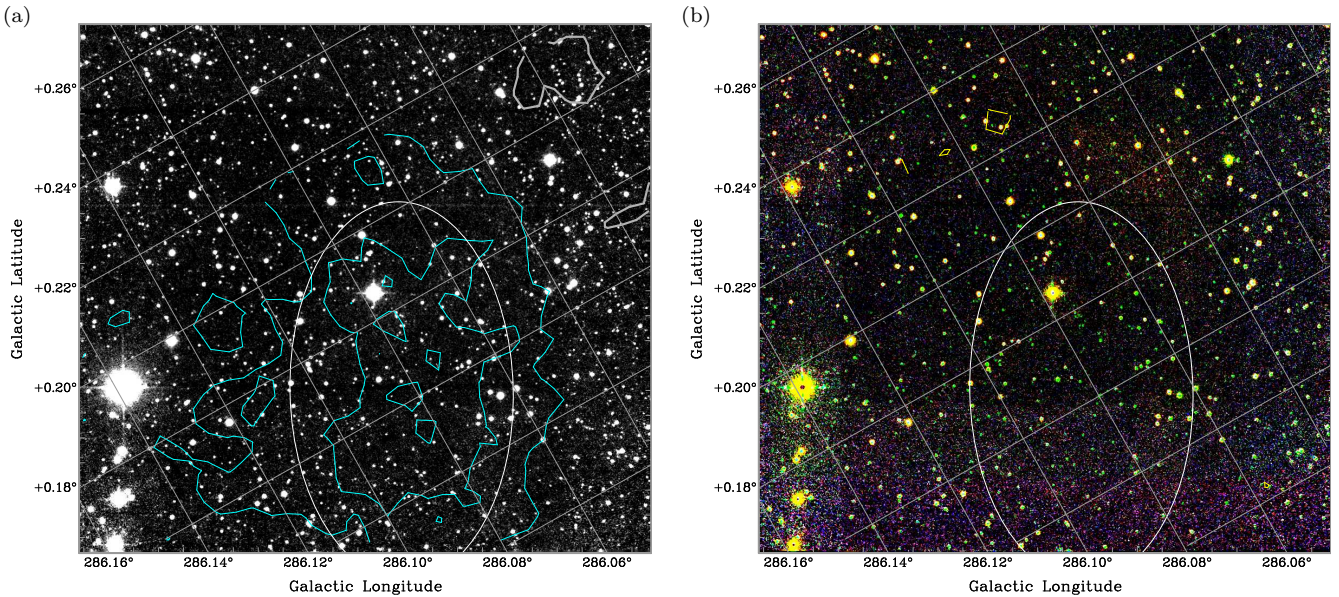


Figure A12. Same as Fig. 2, but for BYF 68 (part of Region 9 from Paper I, see Fig. 1). (a) K -band line-free continuum image with HCO^+ contours (heavy grey at 0 and cyan at 6, 10, and 14 times the rms level of $0.404 \text{ K km s}^{-1}$). (b) RGB-pseudo-colour image of the continuum-subtracted K -band spectral lines with N_2H^+ contours (grey at -3 and yellow at 3 times the rms level of $0.253 \text{ K km s}^{-1}$). The white ellipse shows a gaussian fit to the HCO^+ emission in both panels. At a distance of 2.5 kpc, the scale is $40'' = 0.485 \text{ pc}$ or $1 \text{ pc} = 0^\circ.0229 = 82''.5$.

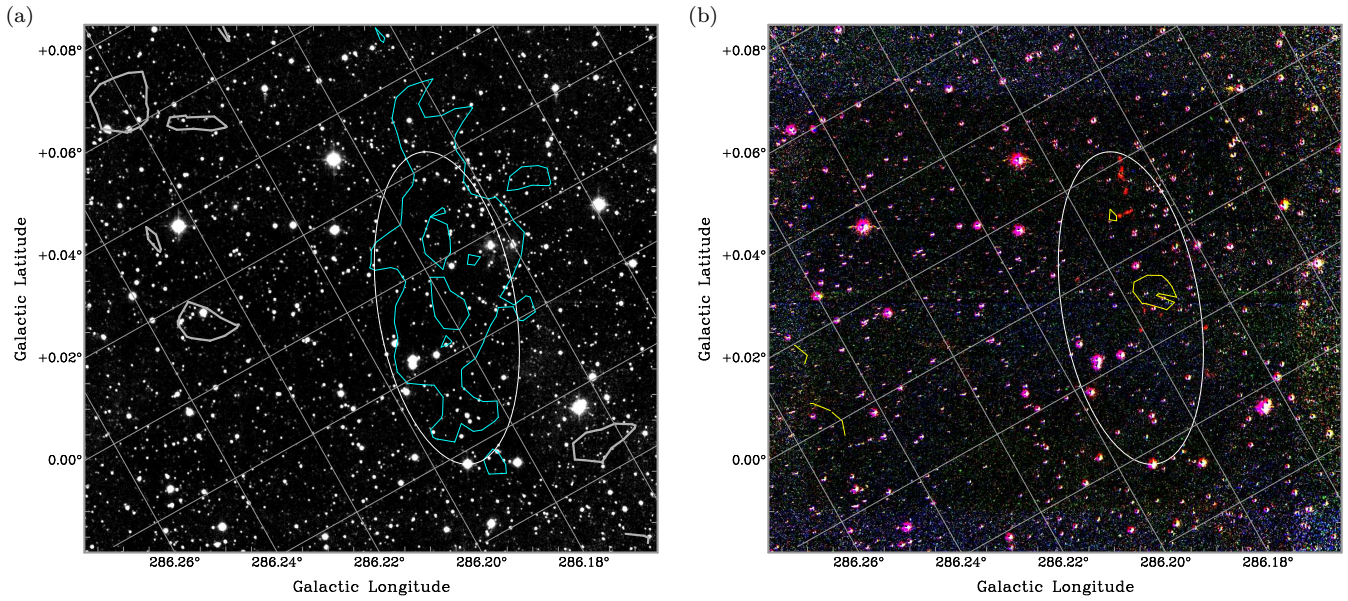


Figure A13. Same as Fig. 2, but for BYF 72 (part of Region 9 from Paper I, see Fig. 1). (a) K -band line-free continuum image with HCO^+ contours (heavy grey at 0 and cyan at 6, 10, and 14 times the rms level of $0.404 \text{ K km s}^{-1}$). (b) RGB-pseudo-colour image of the continuum-subtracted K -band spectral lines with N_2H^+ contours (grey at -3 and yellow at 3 times the rms level of $0.253 \text{ K km s}^{-1}$). The white ellipse shows a gaussian fit to the HCO^+ emission in both panels. At a distance of 2.5 kpc, the scale is $40'' = 0.485 \text{ pc}$ or $1 \text{ pc} = 0^{\circ}.0229 = 82''.5$.

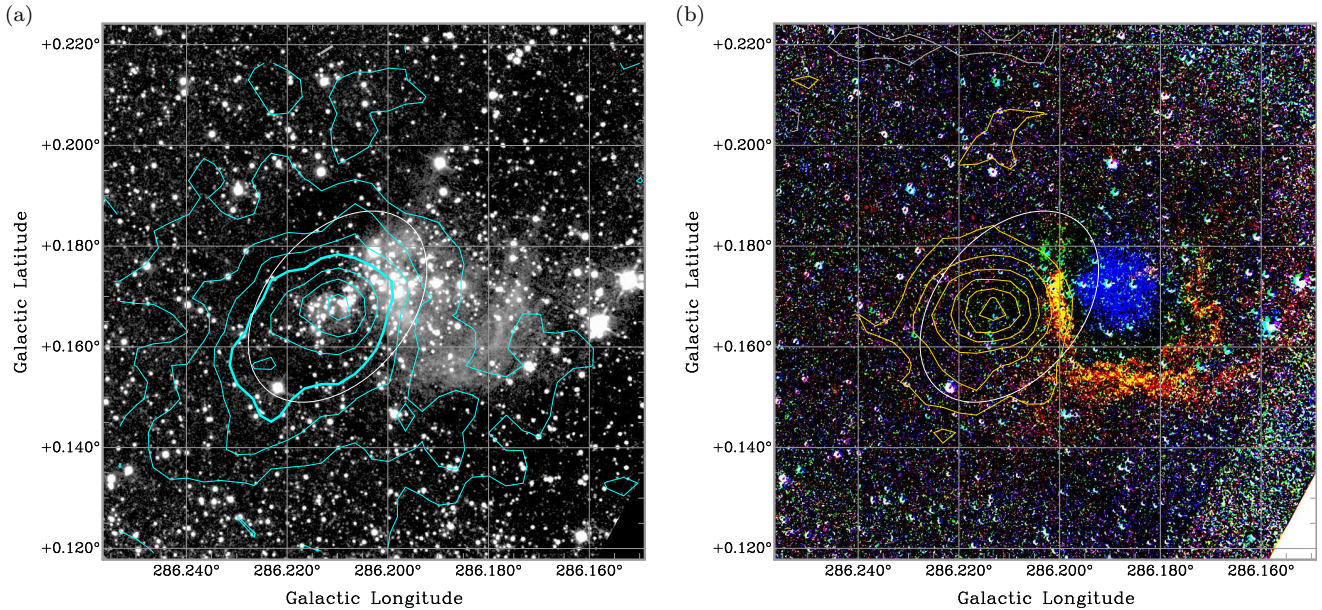


Figure A14. Same as Fig. 2, but for BYF 73 (part of Region 9 from Paper I, see Fig. 1) using more sensitive 2006 data. (a) K -band line-free continuum image with HCO^+ contours (heavy grey at 0, cyan at 6, 9, 12, 15 (heavy), 19, 22.5, and 26 times the rms level of $0.404 \text{ K km s}^{-1}$). (b) RGB-pseudo-colour image of the continuum-subtracted K -band spectral lines with N_2H^+ contours (grey at -3 and -6 , yellow at 3, 6, ..., 15, and 18 times the rms level of $0.253 \text{ K km s}^{-1}$). The white ellipse shows a gaussian fit to the HCO^+ emission in both panels. At a distance of 2.5 kpc, the scale is $40'' = 0.485 \text{ pc}$ or $1 \text{ pc} = 0^{\circ}.0229 = 82''.5$. Note that Fig. 7a in Barnes et al. (2010) has the colour assignments of the H_2 lines switched; this error is corrected in (b).

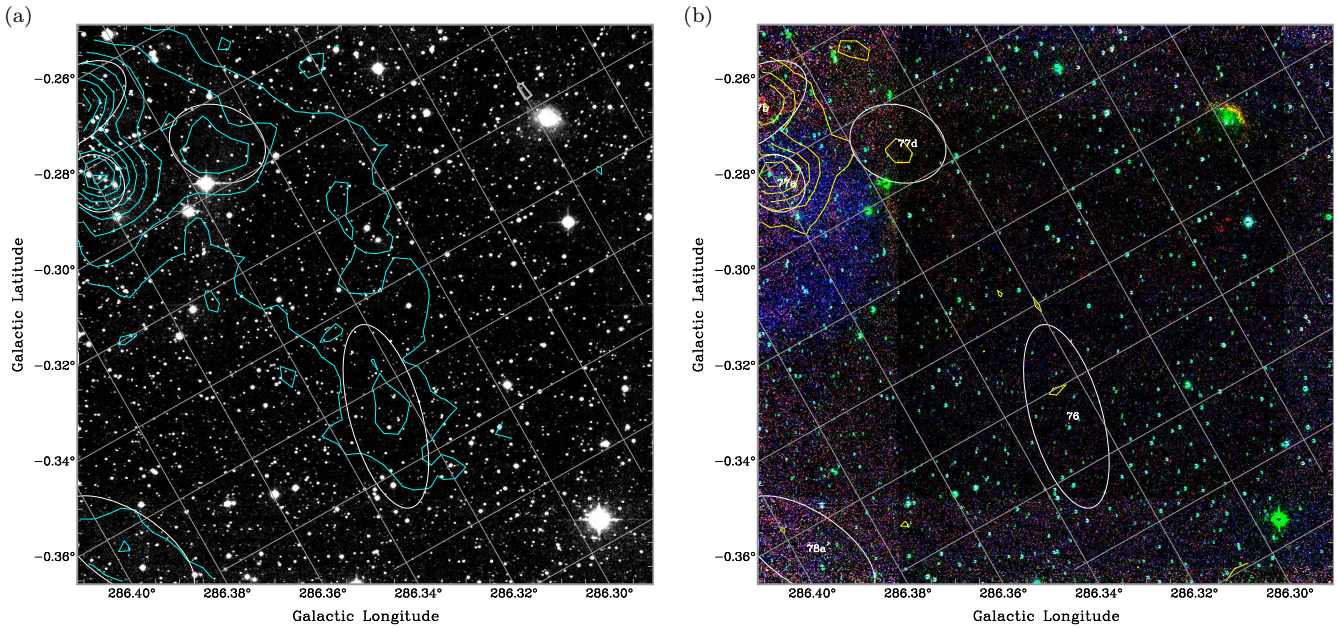


Figure A15. Same as Fig. 2, but for BYF 76–78 (part of Region 9 from Paper I, see Fig. 1). (a) *K*-band line-free continuum image with HCO^+ contours (heavy grey at 0 and cyan at 6, 10, and 14 times the rms level of $0.404 \text{ K km s}^{-1}$). (b) RGB-pseudo-colour image of the continuum-subtracted *K*-band spectral lines with N_2H^+ contours (grey at -3 and yellow at 3 times the rms level of $0.253 \text{ K km s}^{-1}$). White ellipses show gaussian fits to the HCO^+ emission in both panels. At a distance of 2.5 kpc, the scale is $40'' = 0.485 \text{ pc}$ or $1 \text{ pc} = 0^\circ 0229 = 82''.5$.

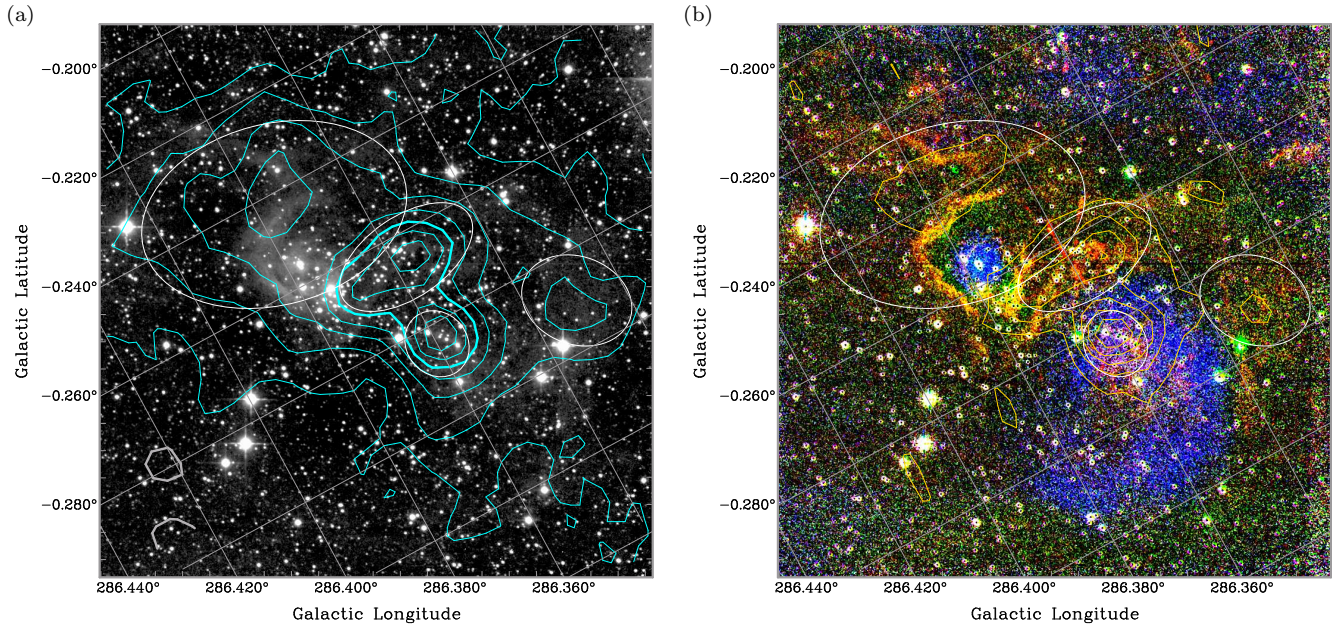


Figure A16. Same as Fig. 2, but for BYF 77 (part of Region 9 from Paper I, see Fig. 1) using more sensitive 2006 data. (a) *K*-band line-free continuum image with HCO^+ contours (heavy grey at 0, cyan at 5, 10, 15, 20, 25(heavy), 30, and 35 times the rms level of $0.404 \text{ K km s}^{-1}$). (b) RGB-pseudo-colour image of the continuum-subtracted *K*-band spectral lines with N_2H^+ contours (grey at -3 and -6 , yellow at 3, 6, 9, 12, and 15 times the rms level of $0.253 \text{ K km s}^{-1}$). White ellipses show gaussian fits to the HCO^+ emission in both panels. At a distance of 2.5 kpc, the scale is $40'' = 0.485 \text{ pc}$ or $1 \text{ pc} = 0^\circ 0229 = 82''.5$.

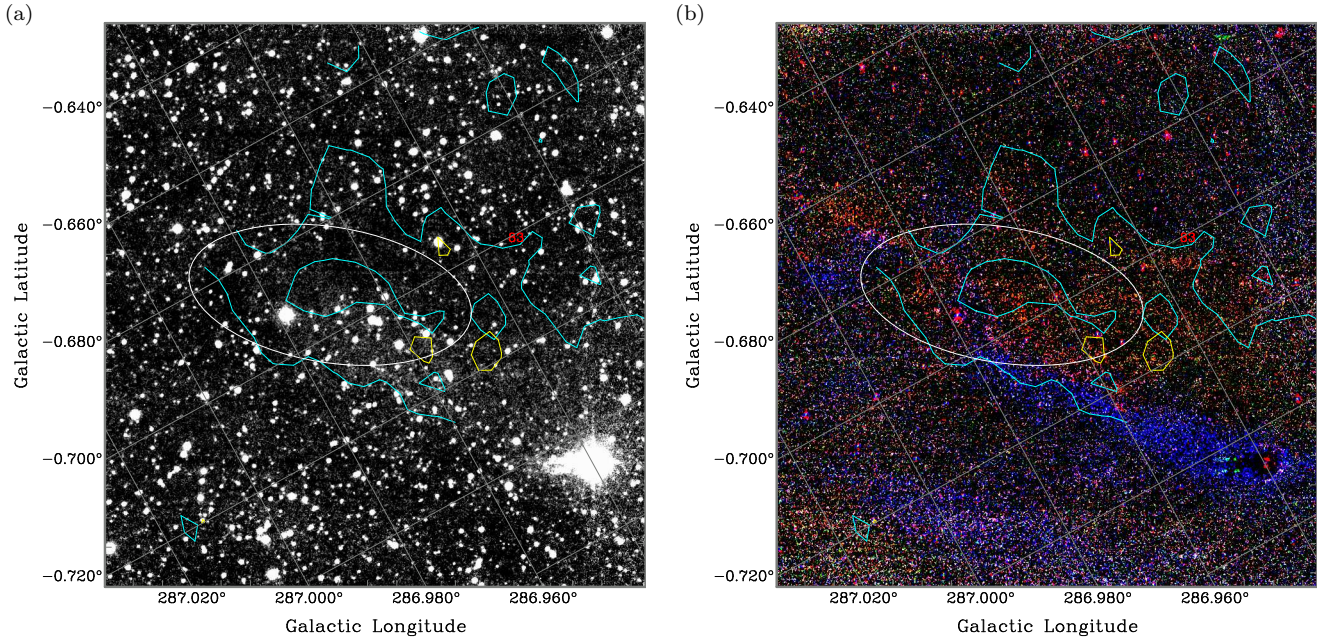


Figure A17. Same as Fig. 2, but for BYF 83 (part of Region 10 from Paper I). (a) K -band line-free continuum image with both HCO^+ contours (cyan at 4 and 8 times the rms level of $0.373 \text{ K km s}^{-1}$) and N_2H^+ contours (yellow at 3 times the rms level of $0.378 \text{ K km s}^{-1}$). (b) RGB-pseudo-colour image of the continuum-subtracted K -band spectral lines with the same contours as in (a). The white ellipse shows a gaussian fit to the HCO^+ emission in both panels. At a distance of 2.5 kpc, the scale is $40'' = 0.485 \text{ pc}$ or $1 \text{ pc} = 0^{\circ}0229 = 82''5$.

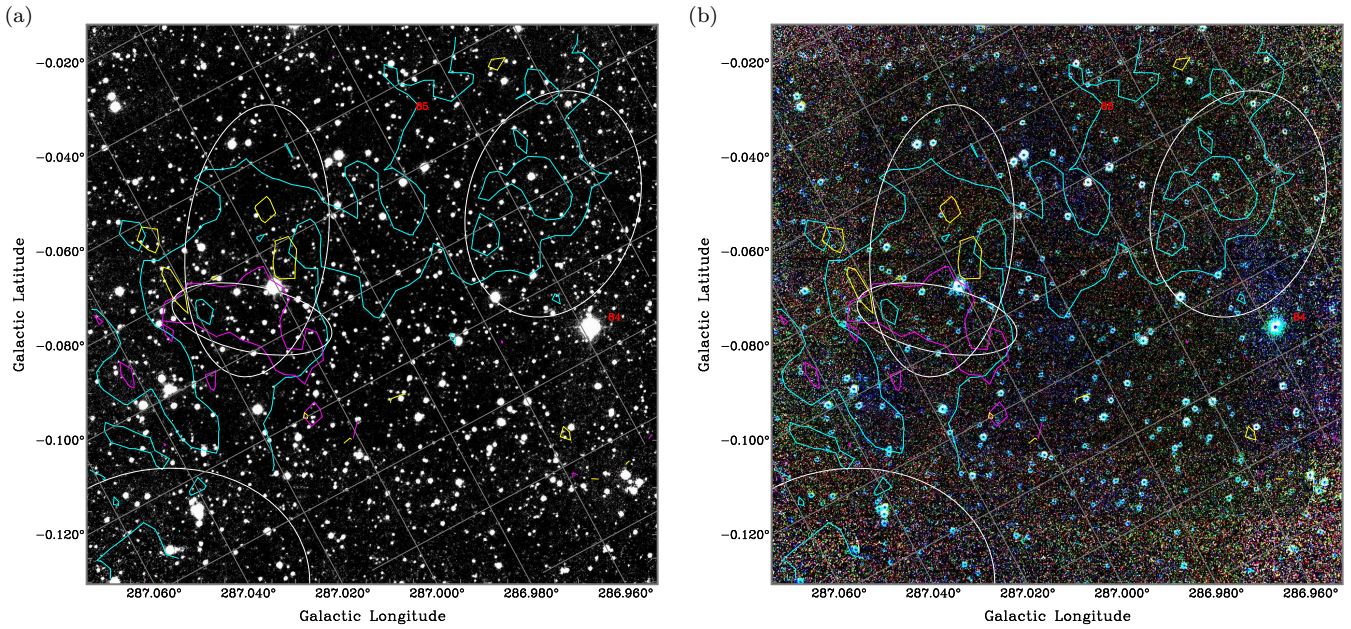


Figure A18. Same as Fig. 2, but for BYF 85 (part of Region 10 from Paper I). (a) K -band line-free continuum image. In this field we show three sets of contours since there are two velocity components visible in the HCO^+ data. At $V_{\text{LSR}} = -20 \text{ km s}^{-1}$ are cyan HCO^+ contours (at 4 and 8 times the rms level of $0.329 \text{ K km s}^{-1}$) and yellow N_2H^+ contours (at 3 times the rms level of $0.332 \text{ K km s}^{-1}$). At $V_{\text{LSR}} = -9 \text{ km s}^{-1}$ are magenta HCO^+ contours (at 3 times the rms level of $0.313 \text{ K km s}^{-1}$). (b) RGB-pseudo-colour image of the continuum-subtracted K -band spectral lines with the same contours as in (a). White ellipses show gaussian fits to the HCO^+ emission in both panels. At a distance of 2.5 kpc, the scale is $40'' = 0.485 \text{ pc}$ or $1 \text{ pc} = 0^{\circ}0229 = 82''5$.

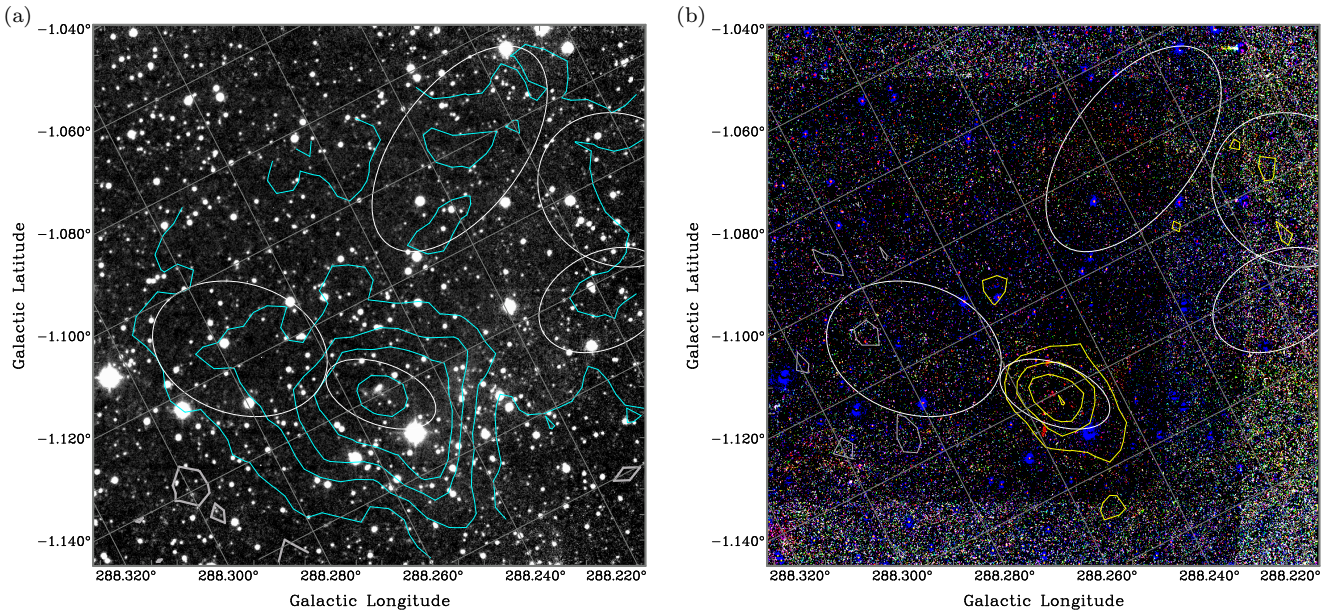


Figure A19. Same as Fig. 2, but for BYF 118 (part of Region 11 from Paper I). (a) K -band line-free continuum image with HCO^+ contours (heavy grey at 0, cyan at 5, 10 15, 20, and 40 times the rms level of $0.237 \text{ K km s}^{-1}$). (b) RGB-pseudo-colour image of the continuum-subtracted K -band spectral lines with N_2H^+ contours (grey at -3, yellow at 3, 6, 9, and 12 times the rms level of $0.217 \text{ K km s}^{-1}$). White ellipses show gaussian fits to the HCO^+ emission in both panels. At a distance of 2.5 kpc, the scale is $40'' = 0.485 \text{ pc}$ or $1 \text{ pc} = 0^\circ 0229 = 82''.5$.

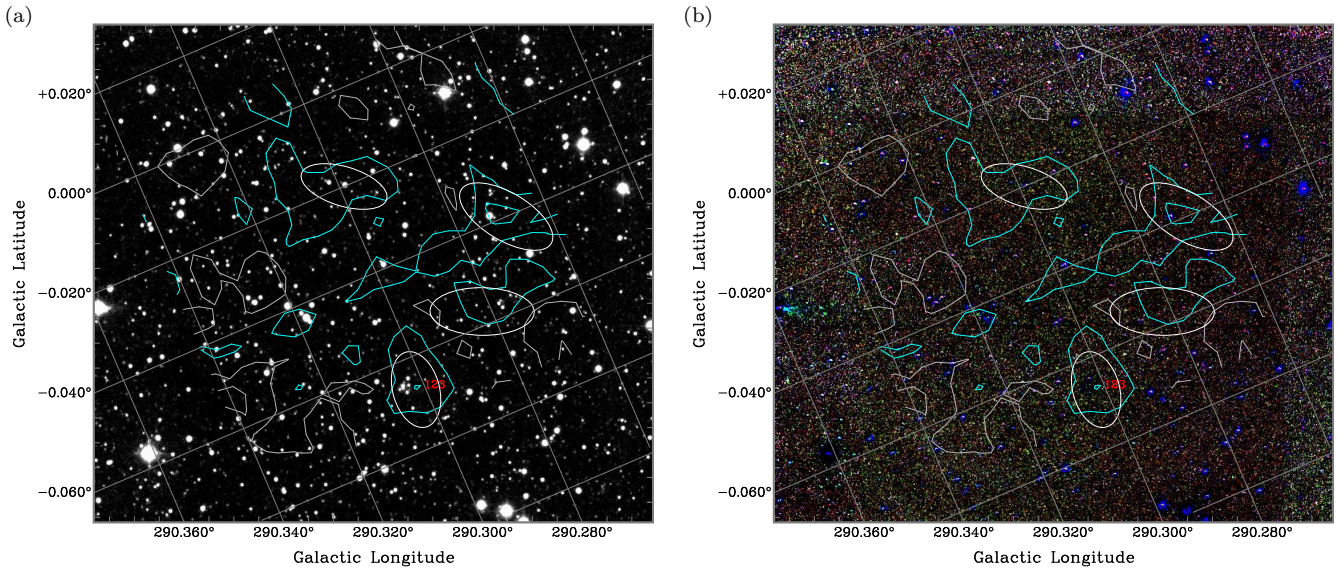


Figure A20. Same as Fig. 2, but for the isolated source BYF 123 from Paper I. (a) K -band line-free continuum image with HCO^+ contours (grey at 0, cyan at 2 and 4 times the rms level of $0.418 \text{ K km s}^{-1}$). (b) RGB-pseudo-colour image of the continuum-subtracted K -band spectral lines with the same contours as in (a). (No N_2H^+ data are available for this field.) White ellipses show gaussian fits to the HCO^+ emission in both panels. At a distance of 6.8 kpc, the scale is $40'' = 1.32 \text{ pc}$ or $1 \text{ pc} = 0^\circ 0084 = 30''.3$.

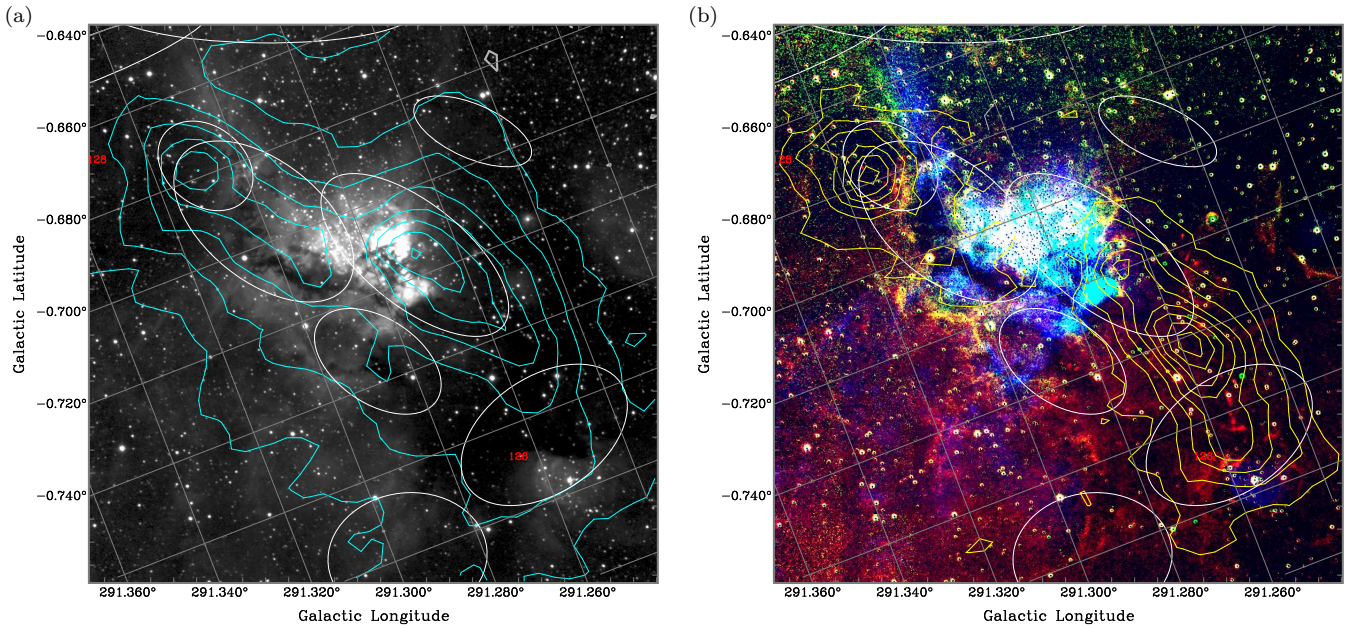


Figure A21. Same as Fig. 2, but for BYF 126 and 128, also known as NGC 3576 (part of Region 13 from Paper I) (a) K -band line-free continuum image with HCO^+ contours (heavy grey at 0, cyan at 10, 20, ..., 60, and 70 times the rms level of $0.424 \text{ K km s}^{-1}$). (b) RGB-pseudo-colour image of the continuum-subtracted K -band spectral lines with N_2H^+ contours (grey at -4 , yellow at 4, 8, ..., 28, and 32 times the rms level of $0.386 \text{ K km s}^{-1}$). White ellipses show gaussian fits to the HCO^+ emission in both panels. At a distance of 2.4 kpc , the scale is $40'' = 0.465 \text{ pc}$ or $1 \text{ pc} = 0^\circ 0239 = 85''.9$.

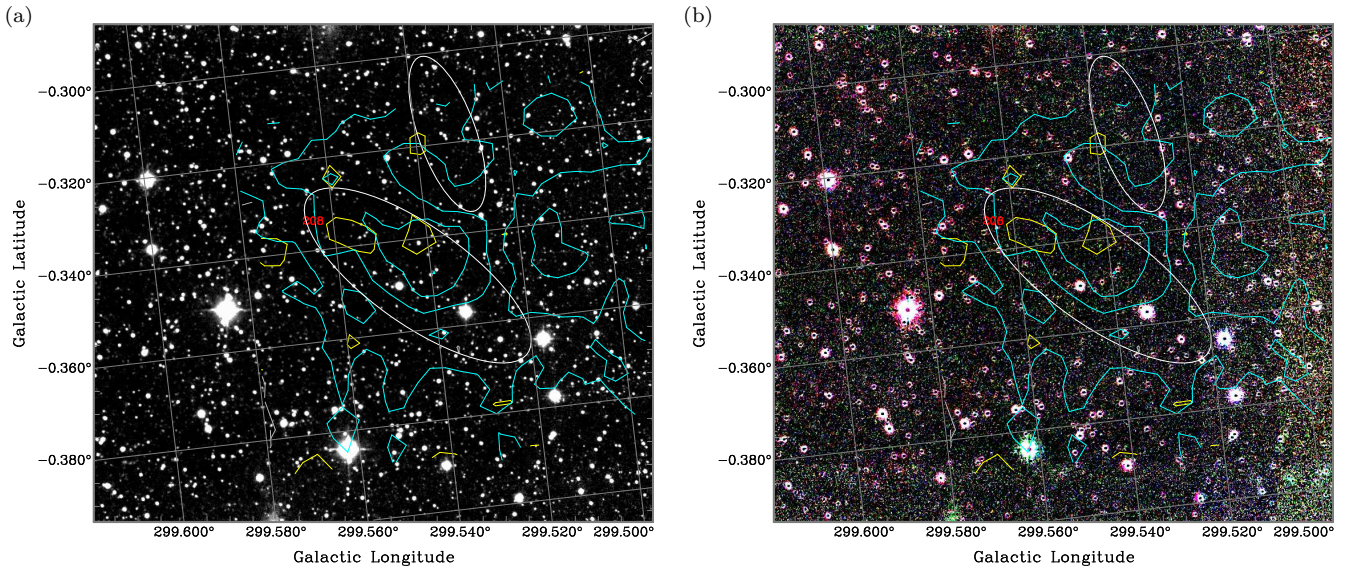


Figure A22. Same as Fig. 2, but for BYF 208 (part of Region 26 from Paper I). (a) K -band line-free continuum image with both HCO^+ contours (grey at -3 , cyan at 3, 6, and 9 times the rms level of $0.230 \text{ K km s}^{-1}$) and N_2H^+ contours (grey at -2.5 and yellow at 2.5 times the rms level of $0.199 \text{ K km s}^{-1}$). (b) RGB-pseudo-colour image of the continuum-subtracted K -band spectral lines with the same contours as in (a). White ellipses show gaussian fits to the HCO^+ emission in both panels. At a distance of 4.7 kpc , the scale is $40'' = 0.911 \text{ pc}$ or $1 \text{ pc} = 0^\circ 0122 = 43''.9$.